Chemical Engineering Journal 527 (2026) 171758

Contents lists available at ScienceDirect

Chemical Engineering Journal

journal homepage: www.elsevier.com/locate/cej

Steering the $Bi_4Ti_3O_{12}$-to-$SrTiO_3$ hydrothermal transformation for controlling the functionality of two-dimensional (2D) $SrTiO_3$ nanoplatelets for photocatalytic H_2 evolution

Marjeta Maček Kržmanc [a,*], Nina Daneu [a,b], Khaja Mohaideen Kamal [c], Blaž Likozar [c], Alja Čontala [a,b], Matjaž Spreitzer [a,b], Jeffrey C.S. Wu [d,*], Suraj Gupta [a,b]

[a] Advanced Materials Department, Jožef Stefan Institute, Jamova cesta 39, 1000, Ljubljana, Slovenia
[b] Jožef Stefan International Postgraduate School, Jamova cesta 39, 1000, Ljubljana, Slovenia
[c] Department of Catalysis and Chemical Reaction Engineering, National Institute of Chemistry, Hajdrihova 19, 1000, Ljubljana, Slovenia
[d] Department of Chemical Engineering, National Taiwan University, Taipei, 10617, Taiwan

ARTICLE INFO

Keywords:
$SrTiO_3$ nanoplatelets
Hydrothermal transformation
Photocatalytic H_2 generation
Aurivillius phase $Bi_4Ti_3O_{12}$

ABSTRACT

The Aurivillius-Phase $Bi_4Ti_3O_{12}$ platelets are not only important functional materials in their own right, but also serve as valuable two-dimensional (2D) templates for converting into 2D $ATiO_3$ (A = Sr, Ba, Ca) perovskite platelets with a favourable (100) orientation. The transformation under low-temperature (200 °C) hydrothermal conditions has recently been demonstrated; however, the process remains underexplored regarding the mechanistic control of the final product properties. This study sheds light on the steering of the $Bi_4Ti_3O_{12}$-to-$SrTiO_3$ hydrothermal transformation to precisely control the surface roughness and photocatalytic properties of the 2D epitaxial heterostructural $SrTiO_3/Bi_4Ti_3O_{12}$ and $SrTiO_3$ nanoplatelets. A higher excess of Sr (Sr/Ti = 15), smaller $Bi_4Ti_3O_{12}$ template nanoplatelets, and pre-reaction etching of the template with hot NaOH promote the formation of high-surface-area $SrTiO_3/Bi_4Ti_3O_{12}$ and $SrTiO_3$ nanoplatelets (BET >60 m^2/g), which show more than 50 times higher H_2 evolution rates compared to smooth, low surface area platelets (BET~10 m^2/g). This study demonstrated that higher surface roughness facilitates effective surface trapping of bismuth species, which, through in-situ reduction to metallic Bi° single atoms, acted as a co-catalyst and enhanced photocatalytic H_2 evolution. Both $SrTiO_3/Bi_4Ti_3O_{12}$ and $SrTiO_3$ nanoplatelets exhibited stable photocatalytic responses, but only $SrTiO_3$ maintained structural and chemical integrity under illumination. This study presents a new strategy for engineering the surface and functional properties of 2D $SrTiO_3$ perovskite nanoplatelets through the hydrothermal transformation of Aurivillius phase $Bi_4Ti_3O_{12}$ nanoplatelets, thereby expanding possibilities for the functional engineering of other 2D perovskite nanostructures.

1. Introduction

Science and technology face significant expectations in the race to tackle global challenges related to climate change, pollution, and the depletion of energy resources. Part of the scientific efforts focus on utilising solar energy to produce alternative fuels and degrade organic pollutants. Over the past 15 years, hydrogen (H_2) fuel produced using sunlight has gained considerable attention as a promising pathway towards a low-carbon future. Among the various solar-driven methods for H_2 production (photoelectrochemical, photovoltaic-electrochemical approaches, etc.), the photocatalytic process stands out for its simplicity, low cost, and suitability for scaling up [1]. However, several challenges remain unresolved, including low sunlight conversion efficiency, limited photocatalyst stability, and the need for effective separation of hydrogen (H_2) and oxygen (O_2). These issues persist despite extensive research efforts, hindering the commercialisation of this promising technology [2,3].

Given the vast number of photocatalytic studies conducted over the last 20 years, it is evident that the breakthrough in the practical exploitation of the photocatalytic processes cannot occur through serendipitous photocatalyst discovery alone, but must arise from knowledge-driven design. Architectures such as 2D/2D epitaxial

* Corresponding authors.
E-mail addresses: marjeta.macek@ijs.si (M.M. Kržmanc), cswu@ntu.edu.tw (J.C.S. Wu).

https://doi.org/10.1016/j.cej.2025.171758
Received 16 September 2025; Received in revised form 16 November 2025; Accepted 9 December 2025
Available online 10 December 2025

heterojunctions with direct *Z*-scheme charge transfer, combined with single-atom co-catalysts, represent state-of-the-art approaches that can simultaneously overcome several bottlenecks in photocatalytic performance [4,5]. The rational design of 2D nanostructures and 2D/2D epitaxial heterostructures can be achieved by converting suitable 2D template precursors under low-temperature hydrothermal conditions that promote dissolution-mediated epitaxial reconstruction. The choice of 2D templates is generally limited to nanostructures that naturally tend to grow anisotropically, a property influenced by their crystal structure. Layered crystal structures, distinguished by the exchange of various structural units, are among the most favourable templates for transforming into new 2D or 2D/2D materials. Besides structural compatibility with the target material, the success of the transformation also relies on the relative solubilities and stabilities of all participating structures under the given conditions [6–9].

Aurivillius phases ((Bi_2O_2) $(A_{n-1}B_nO_{3n+1})$) exemplify spontaneously forming layered 2D (nano)structures, where pseudo-perovskite blocks exchange with $(Bi_2O_2)^{2+}$ layers [10]. These 2D materials have been extensively studied for preparing 2D perovskite platelets through topochemical transformation [11–14]. $Bi_4Ti_3O_{12}$, composed of alternating $(Bi_2Ti_3O_{10})^{2-}$ blocks and $(Bi_2O_2)^{2+}$ layers, is an example of the Aurivillius phase. Due to this layered structure, it naturally grows in anisotropic shapes of (nano)platelets [15–18]. Thanks to this specific crystal structure and the favourable topochemical transformation chemistries in different reaction media, $Bi_4Ti_3O_{12}$ (nano)platelets also provide versatile opportunities for engineering 2D $ATiO_3$ (A = Ba, Sr, Ca) perovskites. Until recently, this type of transformation was mainly studied in molten salt media [10–14]. Our group first reported the transformation of $Bi_4Ti_3O_{12}$ nanoplatelets into $SrTiO_3/Bi_4Ti_3O_{12}$ heterostructures and $SrTiO_3$ nanoplatelets under low-temperature hydrothermal conditions [6,7,19]. Following our example, but with an innovative modification involving the addition of sodium oleate— which significantly altered the conversion mechanism— Wu et al. also prepared $BaTiO_3$ and $Ba_{1-x}Sr_xTiO_3$ platelets through the hydrothermal transformation of $Bi_4Ti_3O_{12}$ platelets [20–22].

Despite a relatively large band gap of 3.2 eV, which limits the use of only the ultraviolet part of the solar spectrum (just 5 %), $SrTiO_3$ has been widely researched as a photocatalyst for H_2 evolution, mainly because of its low cost and photo-corrosion stability. The highest quantum efficiency of nearly 1 and the largest scale-up of sunlight-driven H_2 generation were achieved precisely by cube-like Al-doped $SrTiO_3$ particles loaded with Rh/Cr_2O_3 and CoOOH cocatalysts [2,3]. These studies support further research into $SrTiO_3$ nanostructures in the field of photocatalytic H_2 evolution, especially those with more optimal 2D nanostructures, which are of significant interest.

Continuing our previous investigations on the hydrothermal $Bi_4Ti_3O_{12}$-to-$SrTiO_3$ transformation, this work provides the first evidence that the transformation pathway can be intentionally steered to tailor the morphology, surface area, and functional properties of the transformed 2D/2D $SrTiO_3/Bi_4Ti_3O_{12}$ and 2D $SrTiO_3$ nanostructures. We present two distinct experimental strategies that yielded significant differences in surface roughness and, correspondingly, in their contrasting photocatalytic performances. We demonstrated that rough, high surface-area $SrTiO_3$ nanoplatelets derived from $Bi_4Ti_3O_{12}$ efficiently expose a small amount of remaining bismuth nanospecies at their surfaces, which can be in-situ photo-reduced into metallic Bi° single atoms, acting as efficient non-noble metal co-catalysts for H_2 evolution.

Moreover, our results emphasise the importance of a thorough understanding and precise control of the synthesis process in the development of nanostructured materials with reproducible and tunable functionalities. This study is not only important for the advancement of $SrTiO_3$-based photocatalysis, but also contributes significantly to the rational design of 2D nanostructures and 2D/2D epitaxial heterostructures through low-temperature hydrothermal topochemical transformation.

2. Experimental

2.1. Synthesis conditions

2.1.1. Chemicals

All chemicals were used as received without further purification. KCl (Sigma-Aldrich, ≥99.0 %), NaCl (Merck, ≥99.7 %), Bi_2O_3 nanopowder (Alfa Aesar, 99.8 %), TiO_2 (P25, Degussa), $SrCl_2•6H_2O$ (Sigma-Aldrich, ≥99.0 %), NaOH (Fisher Chemicals, ≥98.7 %), HNO_3 (VWR, 68 %). The water, that we used in the synthesis processes, was purified with a system to produce 18.2 MΩ.cm ultra-pure water (Purelab Option-Q7, ELGA).

2.1.2. Synthesis of the $Bi_4Ti_3O_{12}$ template nanoplatelets

The $Bi_4Ti_3O_{12}$ template platelets were synthesised using the molten salt method, as described in our previous reports [6,7,11,12,19]. In brief, we thoroughly mixed TiO_2 and Bi_2O_3 nanopowders with NaCl and KCl salts in the molar ratio of NaCl:KCl:Bi_2O_3:TiO_2 = 50:50:2:3. The powder mixture was placed in an Al_2O_3 crucible, covered, and heated above the salts' melting temperature using three different temperature programmes. The purpose of employing different heating regimes was to produce $Bi_4Ti_3O_{12}$ platelets with varying size distributions. The first programme involved heating at a rate of 10 °C/min to 800 °C, followed by a 2-hour annealing at this temperature, then cooling at 10 °C/min to room temperature. This process is referred to as 800 °C/2 h (see Table S1 and Table S2). A similar process with a shorter 1-hour anneal was labelled 800 °C/1 h. The third annealing programme included heating at 10 °C/min to 800 °C, cooling at 10 °C/min to 700 °C, holding for 2 h at this temperature, then reheating at 10 °C/min to 800 °C, and finally slowly cooling at 1 °C/min to 500 °C, followed by uncontrolled cooling to room temperature. This sequence is abbreviated as 800 °C–700 °C/2 h-800 °C (see Table S2). After each heating cycle, reaction products were separated from the salts by dissolving the salts in water. The resulting powders were then soaked in 2 M HNO_3 for 10 min to remove any residual secondary phases. The powders were repeatedly washed with water to eliminate any remaining HNO_3. The pure $Bi_4Ti_3O_{12}$ platelets were obtained after freeze-drying.

2.1.3. Hydrothermal transformation of the $Bi_4Ti_3O_{12}$ template nanoplatelets into heterostructural $SrTiO_3/Bi_4Ti_3O_{12}$ and $SrTiO_3$ nanoplatelets

The hydrothermal topochemical conversion process from our previous reports was further examined to explore different experimental conditions for adjusting the functional properties [6,7,19]. In the present study, the hydrothermal transformation was performed using two different, carefully controlled procedures, Procedure 1 and Procedure 2. In the initial stage, which was similar for both procedures, $Bi_4Ti_3O_{12}$ platelets and $SrCl_2·6H_2O$ were mixed with a small amount of water, necessary for dissolving the salt. The suspension was sonicated for 20 min, after which it was transferred to the PTFE insert, and the residue was washed with a minimal amount of water. NaOH solution was prepared separately in a flask. Although the procedures differed in the concentrations and temperatures of the initially added NaOH, the final NaOH concentration in the autoclave was the same (6 M). The concentrations of all reagents in the autoclaves, together with other data (Sr/Ti ratios, size of the $Bi_4Ti_3O_{12}$ template nanoplatelets), are summarised in Table S1 and Table S2. The main differences between the procedures are described as follows. In Procedure 1, all reagents were cooled to room temperature before being combined. The initial NaOH solution prepared was less concentrated (6.2 mol/l), and only a few millilitres of water were needed to fill 70 % of the autoclave volume. The heating process began immediately after mixing the reagents and sealing the autoclave. Procedure 2 relies on the natural formation of hot NaOH during the exothermic dissolution of NaOH in water. This hot and concentrated NaOH (12 M) was then poured over the dispersion of the $Bi_4Ti_3O_{12}$ nanoplatelets in $SrCl_2$ water solution. A certain amount

(approximately 220 ml) of water was added to achieve the target 70 % filling of the autoclave (total PTFE insert volume: 700 ml). At this stage, immediately after mixing the reagents, the suspension temperature was typically 46 °C- 48 °C. The start of heating to the target reaction temperature (i.e., 200 °C) was delayed for approximately 30 min to prolong the etching effect of warm NaOH. During this period, the suspension cooled to approximately 32 °C- 34 °C. The reactions were conducted under stirring conditions (150 rpm) in a Teflon-lined autoclave (BR 700), with heating to the final temperature taking about 2 h, while the reaction time at 200 °C varied from 2.5 to 24 h (see Tables S1 and S2). After cooling the reactor to room temperature, the powder was separated from the alkaline solution by centrifugation. Subsequently, soluble species (Na^+, Cl^-, OH^-, Sr^{2+}) were removed from the reaction product through repeated water washing and centrifugation. Water-insoluble side products, $SrCO_3$ and Bi_2O_3, were dissolved using 1 M HNO_3 (soaking for 5 min). The perovskite platelets were then immediately separated from the acid, followed by water washing to remove residual acid. Non-aggregated, well-separated $SrTiO_3/Bi_4Ti_3O_{12}$ or $SrTiO_3$ platelets were obtained after freeze-drying.

2.2. Characterisation

2.2.1. Structural, morphological, surface and electrochemical characterisation

The crystal structure of the synthesised materials was determined using X-ray diffractometers Bruker AXS D4 Endeavour and Empyrean, Malvern PANalytical, both with CuKα_1 radiation (λ =1.5406 Å). X-ray diffraction (XRD) analysis was conducted on powder samples (randomly oriented platelets) as well as on the oriented platelets on the zero-background Si single-crystalline substrate. The latter samples were prepared by casting droplets of the well-sonicated suspension of the platelets in 2-propanol onto the Si single-crystalline substrate. This method was employed for the quantitative determination of the $SrTiO_3$:$Bi_4Ti_3O_{12}$ ratio in the heterostructures via a calibration curve obtained from XRD measurements of the oriented platelets with known ratios of $SrTiO_3$ and $Bi_4Ti_3O_{12}$. The selected diffraction lines for quantification were (100), (200) for $SrTiO_3$ and (008), (0014) for $Bi_4Ti_3O_{12}$.

The microstructural analyses were carried out using a scanning electron microscope (SEM) (Schottky FEG, Verios HP 4G, Thermofisher, USA). Scanning transmission electron microscopy (STEM) analyses were performed on aberration-corrected microscope ARM 200 CF (Jeol, Japan) operated at 200 kV and equipped with cold field emission gun (FEG) and energy dispersive X-ray (EDX) detector. Bright-field (BF-STEM) and high-angle annular dark-field (HAADF-STEM) images were acquired on an annular detector with inner and outer semi-angles of 11–22 mrad and 68–180 mrad, respectively. For EDX mapping of Bi nanoparticles in $SrTiO_3$ matrix, we used aberration-corrected microscope Spectra 300 (Thermo Fisher, Netherlands) with high-brightness FEG and operated at 200 kV. The microscope is equipped with four 30 mm^2 windowless collimated silicon drift detectors (SDDs) with large 0.7 sr solid angle (Super-X EDXS detector) for fast and precise elemental analysis. For STEM analyses of the platelets in top-view orientation, the samples were dispersed in absolute ethanol and applied onto lacey carbon coated copper grids. For analysis of the platelets in edge-view, the samples were embedded in epoxy resin and thinned to electron transparency by mechanical and ion milling (Gatan PIPS Model 691, USA).

X-ray photo-electron spectroscopy (XPS) measurements were performed using PHI Versaprobe III with Al Kα radiation at 1486.6 eV. The acquired data was analysed using Multipak software (PHI) while using C1s peak at 284.8 eV as the reference. The photocatalysts after the photocatalytic process were analysed by ex-situ XPS to determine the light-induced changes in the surface elements' chemical states. To preserve the elements' oxidation states, the powders were first separated from the photocatalytic solution under an argon atmosphere, dried under vacuum and then deposited on the XPS sample holder under a nitrogen atmosphere (in dry box). Using this procedure, we tried to avoid the air exposure of the sample after the photocatalytic process. The powders' Brunauer–Emmett–Teller (BET) surface areas were determined by nitrogen adsorption with a Micromeritics Gemini II 2370 nitrogen-adsorption apparatus (Norcross, GA).

The diffuse reflectance spectra of the platelets were measured in the ultraviolet and visible (UV–Vis) spectral range using a spectrophotometer (Shimadzu UV-3600, Tokyo, Japan) equipped with an integrating sphere containing $BaSO_4$ as the standard. The band gap energies were determined from the diffuse reflectance spectra by means of the Tauc method and the Kubelka-Munk function [23].

For photo-electrochemical measurements, a 5 mm L-shaped glassy carbon electrode was used as the working electrode, onto which a catalyst layer was deposited. To prepare the catalyst ink, 3 mg of powdered catalyst was dispersed in a mixed solvent containing 0.75 mL of deionized water, 0.25 mL of 2-propanol, and 10 μL of Nafion, followed by ultrasonic treatment to ensure uniform dispersion. This ink was then drop-casted onto the glassy carbon surface at a loading of 0.3 mg/cm^2. The electrochemical setup also included a graphite rod as the counter electrode and a Mini-HydroFlex reversible hydrogen electrode (Gaskatel) as the reference electrode. A quartz cube reactor, filled with approximately 100 mL of 1 M KOH electrolyte and purged with nitrogen, housed the electrodes. The catalyst surface was illuminated by a 300 W xenon lamp (Newport) equipped with an AM1.5G filter, calibrated to simulate 1 sun (100 mW/cm^2) using a silicon reference cell (Newport). All electrochemical measurements were conducted under illumination using a Gamry 1010E potentiostat. Linear sweep voltammetry (LSV) was performed within the range of 0 to −0.8 V (vs RHE) at a scan rate of 2 mV/s, while electrochemical impedance spectroscopy (EIS) was carried out at a potential of −0.5 V (vs RHE), spanning frequencies from 100 kHz to 1 MHz. Mott Schottky (MS) measurements were performed at a frequency of 1 kHz for all the samples.

2.2.2. Photocatalytic H_2 production test

The photocatalytic H_2 evolution reactions were carried out in a 73-mL quartz photoreactor (23-mL headspace) with an airtight rubber septum at the top and maintained at room temperature (RT). Typically, 20 mg of photocatalyst was suspended in 50 mL of aqueous solution containing 25 % methanol (*v*/v), which served as a hole scavenger, and the suspension was sonicated for 30 min to obtain a well-dispersed particle suspension. This mixture was sealed in a quartz round bottom flask with rubber septum and purged with N_2 gas for 30 min to remove excess oxygen in the reaction mixture. Finally, the sealed flask was illuminated with light for 4 h (Fig. S1). A 300 W Xenon arc lamp (Newport) equipped with an AM 1.5G filter was used to simulate solar irradiation. The irradiance at the sample surface was measured with a calibrated optical power meter (Newport) and found to be 100 mW·cm^{-2}, corresponding to the standard AM 1.5G solar intensity. The spectrum of the Xe lamp with the AM 1.5G filter is also provided, as shown in Fig. S2. Gas products were sampled hourly with a gas-tight syringe to analyse the H_2 content using a gas chromatograph (GC, SRI—8610C) with a thermal conductivity detector (TCD); high-purity nitrogen was used as the carrier gas. The calibration of the GC is described in Supplementary Material (Fig. S3).

The apparent quantum efficiency (AQE) of the reactions was calculated according to the following equation:

$$\text{AQE}\ (\%) = \frac{\text{Number of reacted electrons}}{\textit{Number of incident photons}} \times 100$$

3. Results and discussion

3.1. Structural, microstructural and morphological characterisation

The three varieties of $Bi_4Ti_3O_{12}$ template nanoplatelets, intended for hydrothermal transformation into heterostructural $SrTiO_3/Bi_4Ti_3O_{12}$

Table I
List of the studied $SrTiO_3$ (STO) and $SrTiO_3/Bi_4Ti_3O_{12}$ (STO/BIT) nanoplatelets together with the summary of the experimental synthesis conditions, composition and BET specific surface areas. Denotations Procedure 1 and Procedure 2 refer to two sets of hydrothermal experiments, as described in Section 2.1.3 (Tables S1, S2).

Sample denotation	Synthesised platelet material (template BIT platelet average side length (L))	Hydrothermal conditions (Sr/Ti, c_{NaOH} (mol/l), T/time)	STO/BIT weight ratio	BET (m^2/g)
Procedure 1				
C1	STO/BIT (1.4 μm)	12, 6 M NaOH, 200 °C/2.5 h	0.8/1	6
C2	STO/BIT (1.4 μm)	12, 6 M NaOH, 200 °C/6 h	1.2/1	10
C3	STO (1.4 μm)	12, 6 M NaOH, 200 °C/15 h	$SrTiO_3$	11
C4	STO (1 μm)	15, 6 M NaOH, 200 °C/20 h	$SrTiO_3$	26
Procedure 2				
H1	STO/BIT (1.4 μm)	15, 6 M NaOH, 200 °C/18 h	0.9/1	39
H2	STO/BIT (1 μm)	15, 6 M NaOH, 200 °C/15 h	1/1	64
H3	STO (1 μm)	15, 6 M NaOH, 200 °C/24 h	$SrTiO_3$	61
H4	STO/BIT (0.9 μm)	15, 6 M NaOH, 200 °C/18 h	1.3/1	53

and $SrTiO_3$ nanoplatelets, were synthesised under different molten salt (NaCl/KCl) conditions. All three $Bi_4Ti_3O_{12}$ nanoplatelet types were discrete, well separated, and highly crystalline, exhibiting an orthorhombic crystal structure (space group: B2ab). Variations in their side length distribution resulted from different annealing regimes (Detailed description in Section S1, Figs. S4, S5).

Under highly alkaline (6 M NaOH) conditions combined with a high strontium excess(Sr/Ti = 12–15), the $Bi_4Ti_3O_{12}$-to-$SrTiO_3$ transformation proceeds via $Bi_4Ti_3O_{12}$ dissolution and $SrTiO_3$ epitaxial growth over both basal surface planes of the template platelets, as described in great detail in our previous reports and summarised in Section S2 of Supplementary Material [6,7,24]. Due to the epitaxial growth mechanism, a highly ordered epitaxial interface forms between the $SrTiO_3$ and $Bi_4Ti_3O_{12}$ along the platelets' basal surface planes, as shown in Fig. S6. The transformation mechanism was found to be highly reproducible, although the surface roughness of the growing $SrTiO_3$ varied considerably, depending on strontium excess, template size and quality, and pre-reaction exposure to warm alkaline conditions. The correlations between these experimental parameters and the surface roughness of the forming $SrTiO_3$ were evaluated through eight representative examples, as shown in Table I. The first set of experiments (Procedure 1, samples C1-C4) used cold NaOH solutions (R.T.), while in the second set (Procedure 2, samples H1-H4), the template platelets were subjected to hot $NaOH/Sr(OH)_2$ etching for 30 min before being heated to a target temperature of 200 °C. In both experimental series, the aim was to prepare heterostructural nanoplatelets with a $SrTiO_3$: $Bi_4Ti_3O_{12}$ weight ratio close to 1:1 as well as pure $SrTiO_3$ nanoplatelets. Regardless of the procedure, the orientation of the growing $SrTiO_3$ was (100), as dictated by the (00*l*) orientation of the $Bi_4Ti_3O_{12}$ nanoplatelets. XRD patterns revealed similar diffraction line widths for $SrTiO_3$, irrespective of the experimental conditions (Fig. 1 and Fig. S7).

The most notable differences among the samples were observed in surface roughness. Smooth surface platelets are typically formed in Procedure 1, using larger templates and lower strontium excess (Table I). In contrast, smaller templates combined with higher strontium excess (Sr/Ti = 15), especially in Procedure 2, favoured the formation of rough basal surfaces of formed platelets. Fig. 2 and Fig. 3 show both morphological types of heterostructural and $SrTiO_3$ nanoplatelets, respectively, as seen from SEM and STEM micrographs. Variations in surface roughness were reflected in the BET specific surface area values (Table I). Additional details on structural/morphological analysis, as well as $Bi_4Ti_3O_{12}$-to-$SrTiO_3$ transformation rates under different experimental conditions (side length, Sr/Ti, procedure type) are provided together with the SEM images of all studied samples (Figs. S8 and S9) in the Section S3 Supplementary Information. The porous rough surface of $SrTiO_3$, in some respects, resembles the TiO_2 nanobelts or TiO_2 nanoparticles with nanocavities, which were also studied as photocatalysts [25–28] or for electrochemical lithium storage [29]. The reported nanocavities in TiO_2 nanostructures do not form in the process of epitaxial growth, as is the case with $SrTiO_3$ in our study. The formation of nanocavities in TiO_2 nanobelts was attributed to the removal of water and surface dehydroxylation during annealing of $H_2Ti_3O_7$ nanobelts, while the nanocavities in TiO_2 nanoparticles were correlated with the incorporation of fluorine in the TiO_2 lattice during microwave-assisted hydrolysis and post-annealing.

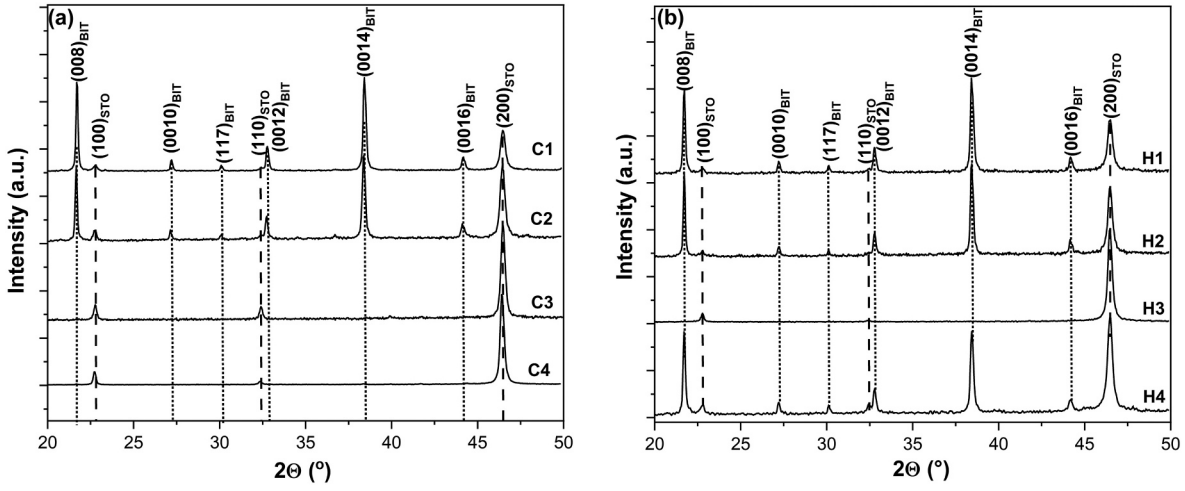

Fig. 1. XRD patterns of the preferentially oriented $SrTiO_3/Bi_4Ti_3O_{12}$ and $SrTiO_3$ platelets (cast on a single-crystalline silicon substrate) synthesised in 6 M NaOH at 200 °C after using different experimental conditions (Table I), as detailed in Experimental Section 2.1.3 in Table S1 (a) and Table S2 (b). As evident from the XRD patterns of the samples denoted by C3, C4, and H3, these are pure $SrTiO_3$, while those marked with C1, C2, H1, H2 and H4 are $SrTiO_3/Bi_4Ti_3O_{12}$ heterostructures. For the indexation of the diffraction patterns, the JCPDS reference cards 01-074-1296 and 01-083-8385 were used for $SrTiO_3$ and $Bi_4Ti_3O_{12}$, respectively.

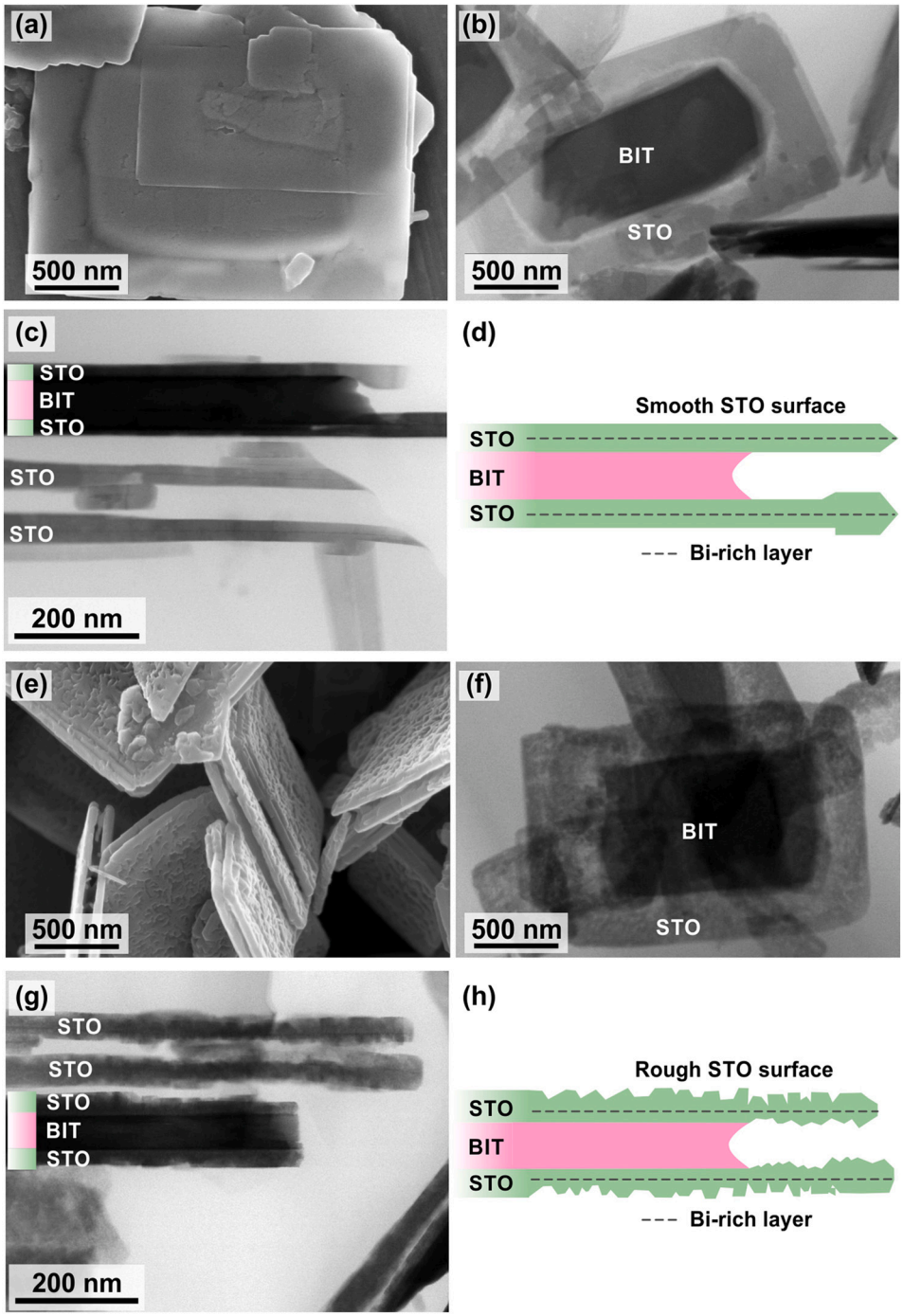

Fig. 2. (a, e) SEM and (b, c, f, g) STEM micrographs of the representative $SrTiO_3/Bi_4Ti_3O_{12}$ platelets, synthesised by Procedure 1 (a-c: Sample C1 in Table I) and by Procedure 2 (e-g: Sample H2 in Table I). The $SrTiO_3/Bi_4Ti_3O_{12}$ platelets, denoted as sample C1 and sample H2 were prepared from the $Bi_4Ti_3O_{12}$ template platelets with the average side length (L) of 1.4 μm and 1 μm, respectively. The Sr/Ti initial molar ratios were 12 and 15 for the samples C1 and H2, respectively. In both cases, $C_{NaOH} = 6$ M and $T = 200$ °C, while the reaction time was 2.5 h for sample C1 (a-c) and 15 h for sample H2 (e-g). (d, h) Schematic presentation of the main difference between the two types of platelets in terms of their surface roughness.

3.2. Surface characterisation by X-ray photoelectron spectroscopy (XPS)

Photocatalytic reactions are surface-controlled processes; therefore, surface characterisation techniques like XPS are vital for clarifying the link between surface chemistry and photocatalytic behaviour. In this study, XPS was used to examine the surface chemical states of the elements constituting the platelets—strontium, titanium, oxygen, and bismuth—both before and after the photocatalytic assessment. It is important to highlight that in this case, the XPS results are not suitable for reliable quantitative analysis of the composition due to the different surface roughness and particular shape of cleaved platelets. Nonetheless, these measurements offer valuable insights into the surface characteristics relevant to the photocatalytic process. The XPS survey scans confirmed the presence of Sr, Ti, O, and Bi in all the as-prepared heterostructural $SrTiO_3/Bi_4Ti_3O_{12}$ and $SrTiO_3$ platelets. With the exception of C, no other foreign element was detected (Fig. S10). Fig. 4 shows the high-resolution XPS spectra for representative heterostructures (Fig. 4a) and pure $SrTiO_3$ nanoplatelets (Fig. 4b). Regardless of the degree of

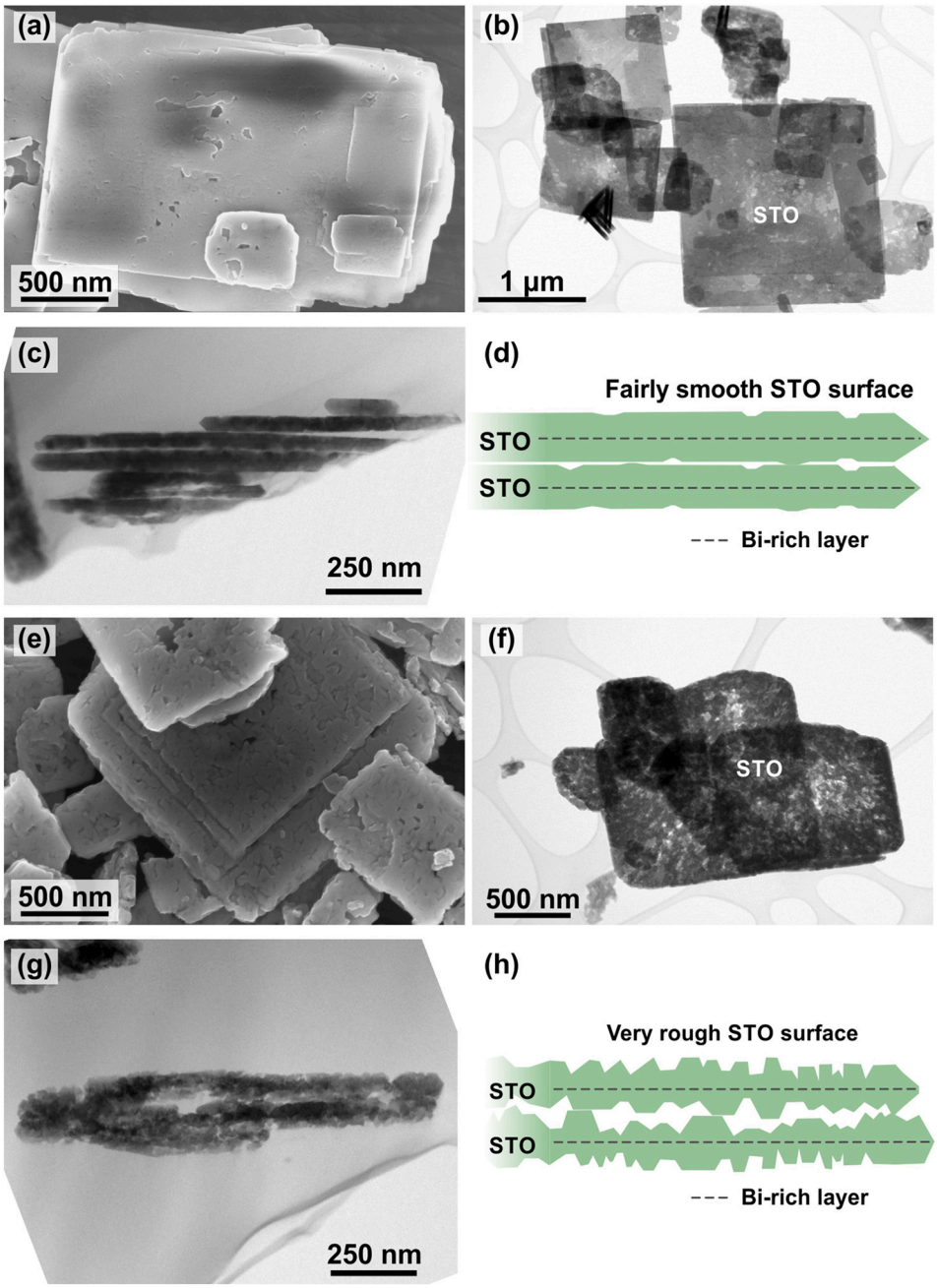

Fig. 3. (a, e) SEM and (b, c, f, g) STEM micrographs of the representative $SrTiO_3$ platelets, synthesised by Procedure 1 (a-c: Sample C3 in Table I) and Procedure 2 (e-g: Sample H3 in Table I). $SrTiO_3$ platelets, denoted as sample C3 and sample H3 were prepared from the $Bi_4Ti_3O_{12}$ template platelets with an average side length of 1.4 μm and 1 μm, respectively. The Sr/Ti initial molar ratios were 12 and 15 for the samples C3 and H3, respectively. In both cases, $C_{NaOH} = 6$ M and $T = 200$ °C, while the reaction time was 15 h for sample C3 (a-c) and 24 h for sample H3 (e-g). (d, h) Schematic presentation of the platelets, completely transformed to $SrTiO_3$ prepared according to the two different procedures, which show significantly different surface roughness that reflects in the difference in BET (Table I).

transformation, Sr 3d XPS spectra of heterostructures and $SrTiO_3$ show peaks at 132.6 eV and 134.4 eV, corresponding to Sr $3d_{5/2}$ and Sr $3d_{3/2}$ states, thus confirming the bonding of Sr^{2+} in $SrTiO_3$. Similarly, the binding energies of Ti $2p_{3/2}$ at 458.2 eV and Ti $2p_{1/2}$ at 464.0 eV indicate the Ti^{4+} oxidation state. The detection of bismuth in $SrTiO_3$ platelets by XPS confirms that during the conversion process, captured and trapped bismuth species are present on or near the surface. The highest intensities of Bi 4f states, appearing at a binding energy of 159.0 eV (Bi $4f_{7/2}$) and 164.0 eV (Bi $4f_{5/2}$), correspond to Bi^{3+} bonded to oxygen. The asymmetry of the Bi 4f peaks demonstrates the presence of metallic Bi°. Obvious shoulder peaks, observed at 157 eV and 162.3 eV in the Bi 4f spectra of the rough surface $SrTiO_3$ (Sample H3) and $SrTiO_3/Bi_4Ti_3O_{12}$ (Sample H2) platelets, indicate higher initial Bi° content at the surface of these platelets compared to those with smooth surfaces and lower BET values (Samples C2, C3 and C4).

3.3. Photocatalytic activity evaluation and stability

The significant contrast in the surface roughness of the platelets initiated an investigation to clarify how these variations influence photocatalytic properties. Several key features, such as the formation of a large contact area in the $SrTiO_3/Bi_4Ti_3O_{12}$ epitaxial heterojunction, surface-trapped bismuth species, and the reported band structure properties of $SrTiO_3$, motivated the assessment of the developed

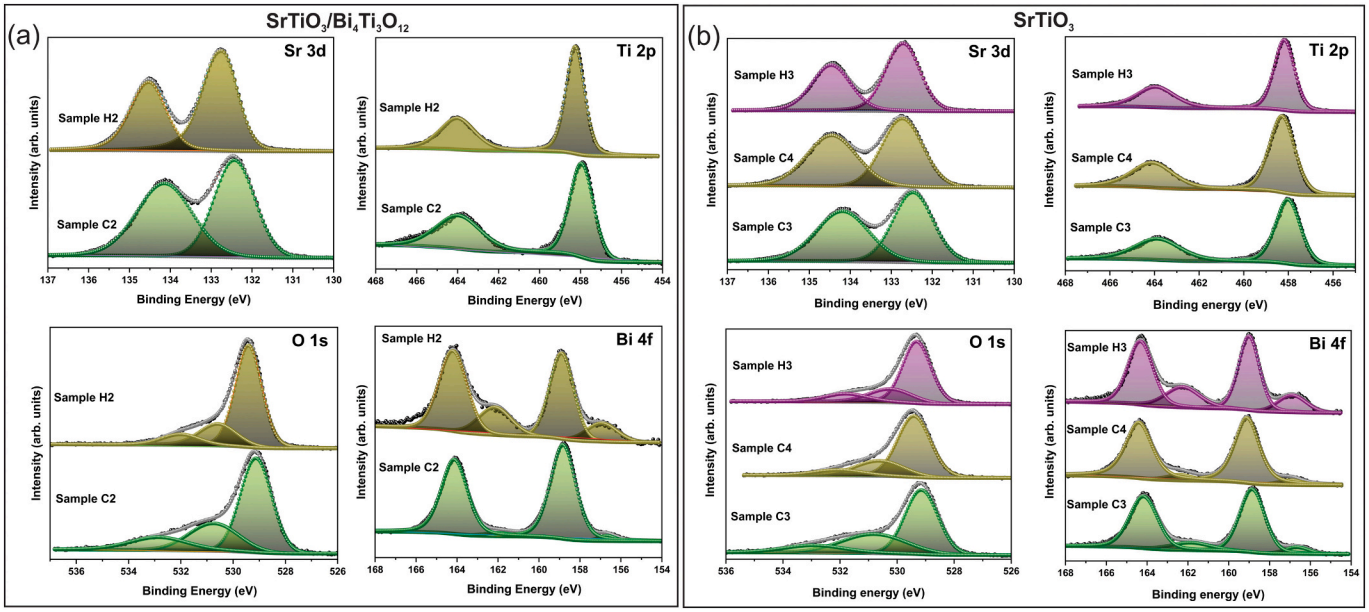

Fig. 4. Comparison of the representative XPS spectra of the as-prepared (a) $SrTiO_3/Bi_4Ti_3O_{12}$ and (b) $SrTiO_3$ nanoplatelets prepared by Procedure 1 (Samples C2, C3, C4) and Procedure 2 (Samples H2 and H3) (Table I).

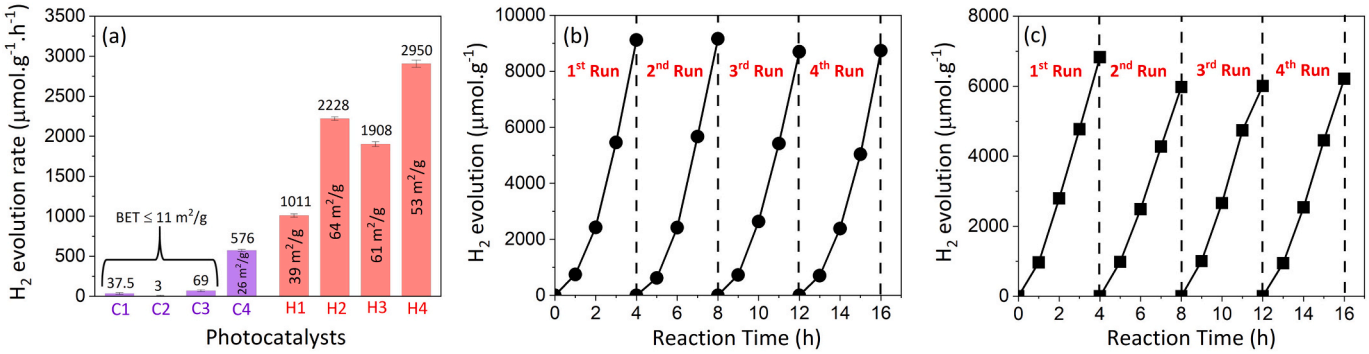

Fig. 5. (a) Rate of H_2 evolution over the $SrTiO_3/Bi_4Ti_3O_{12}$ (samples C1, C2, H1, H2 and H4) and $SrTiO_3$ (samples C3, C4 and H3) nanoplatelets, prepared by Procedure 1 (C1-C4 (violet columns)) and Procedure 2 (H1-H4 (red columns), (b, c) stability test of H_2 evolution: (b) for $SrTiO_3/Bi_4Ti_3O_{12}$ platelets (Sample H2) and (c) for $SrTiO_3$ platelets (Sample H3). Every 4 h reaction, the formed H_2 was evacuated. Photocatalytic experiments were performed for the suspension of photocatalysts (20 mg) in a 50 ml aqueous solution containing 25 vol% of methanol.

nanoplatelets for photocatalytic H_2 evolution. Band gap (Eg) determination from UV-VIS diffuse reflectance spectra using the Tauc method and the Kubelka-Munk function [23] revealed no significant difference between the Eg of the heterostructural platelets and that of the $SrTiO_3$ platelets obtained by the two procedures. The Eg values varied between 3.22 eV and 3.28 eV, as presented in Fig. S11. A Detailed description of the band gap determination is also given in the Supplementary Material. The results of the photocatalytic measurements, shown in Fig. 5 and summarised in Table S3 (Extended Table data of Table I), disclosed significant variation in H_2 evolution rates. No direct correlation was observed between photocatalytic activity and platelet composition. Both pure $SrTiO_3$ platelets and $SrTiO_3/Bi_4Ti_3O_{12}$ platelets demonstrated either high or low H_2 evolution rates. A general observation is that platelets with a smooth surface and BET surface area below 12 m^2/g displayed considerably lower photocatalytic activities compared to those with a rough surface and BET surface area above 50 m^2/g (Table S3). The highest photocatalytic activity was measured for the heterostructure prepared from templates with the widest size distribution and the smallest average side length (Sample H4 in Fig. 5 and Table S3). SEM-backscattered (SEM-BSE) images (Fig. S12) revealed that the sample H4 predominantly consisted of entirely transformed $SrTiO_3$ platelets ($L \leq 1$ μm) with a small content of larger heterostructural platelets (1 μm $< L \leq 3$ μm). Hence, the $SrTiO_3$:$Bi_4Ti_3O_{12}$ weight ratio of 1.3:1 (Table I) does not represent the typical composition of individual platelets but reflects the average composition of the entire H4 sample.

To isolate the effect of the heterojunction, photocatalytic activities were compared for $SrTiO_3$ and heterostructural nanoplatelets, prepared from the same template and with similar surface roughness (BET values). $SrTiO_3$ nanoplatelets (Sample H3) and $SrTiO_3/Bi_4Ti_3O_{12}$ heterostructures (Sample H2) exhibited H_2 evolution rates of 1908 $\mu mol \cdot g^{-1} \cdot h^{-1}$ and 2228 $\mu mol \cdot g^{-1} \cdot h^{-1}$, respectively, with comparable BET values ($SrTiO_3$: 61 m^2/g, $SrTiO_3/Bi_4Ti_3O_{12}$: 64 m^2/g). The results suggest that a large surface area with more active sites plays a significantly more important role in activity than heterojunction formation alone.

Careful monitoring of the photocatalytic processes and a review of the literature can provide better insights into the plausible mechanisms behind the observed variations in activity. The main visual observation was that $SrTiO_3/Bi_4Ti_3O_{12}$ platelets turned black during the photocatalytic process (Fig. S13a), while the active $SrTiO_3$ platelets became brownish-greyish (Fig. S13c and d). However, after exposure to air,

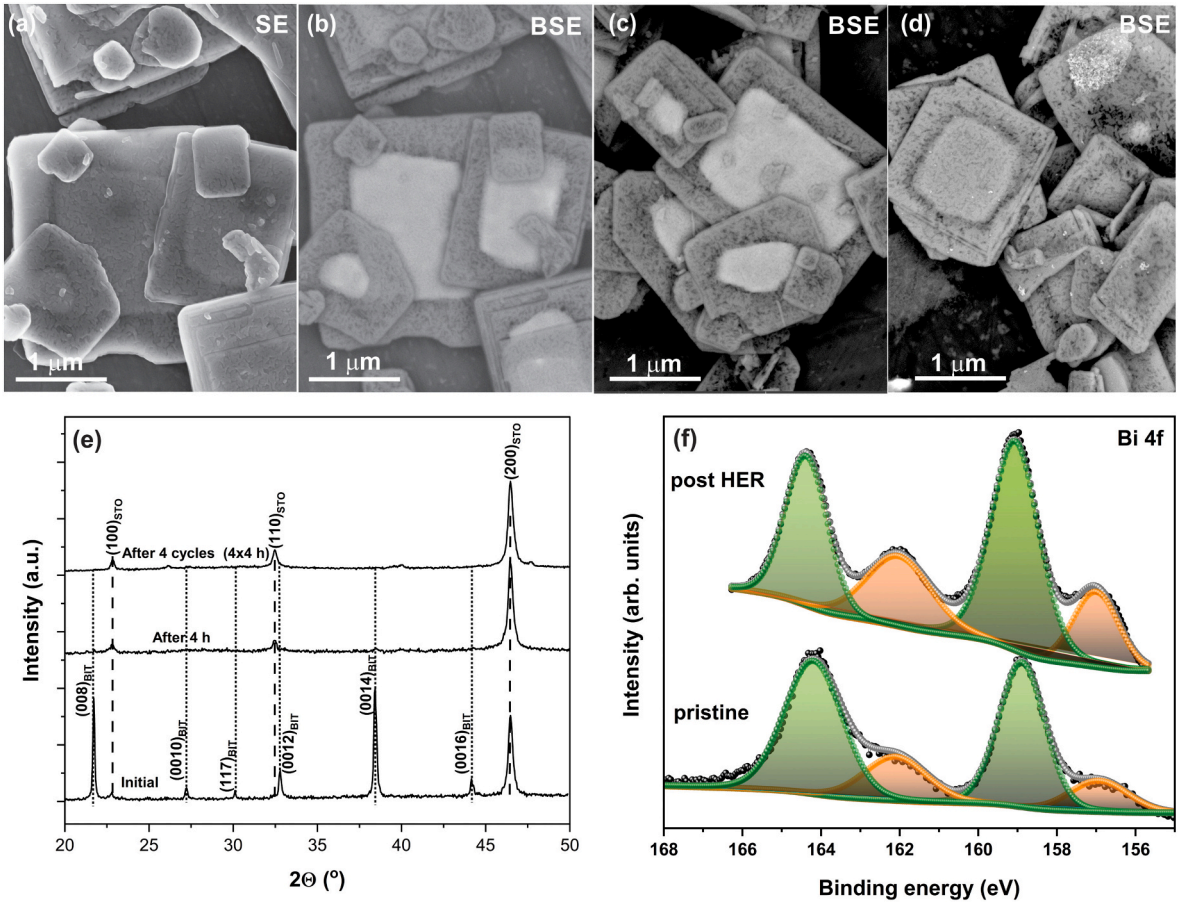

Fig. 6. (a) Secondary electron (SE) and (b, c, d) backscattered electron (BSE) SEM micrographs of (a, b) as-prepared $SrTiO_3/Bi_4Ti_3O_{12}$ platelets (Sample H2) and BSE micrographs of $SrTiO_3/Bi_4Ti_3O_{12}$ platelets (c) after 4-hour photocatalytic H_2 evolution reaction (HER) and (d) after 4 cycles of 4-hour photocatalytic process. (e) Comparison of the XRD pattern of the as-prepared $SrTiO_3/Bi_4Ti_3O_{12}$ platelets (bottom curve) with those after the 4-hour photocatalytic process (middle) and after 4 cycles of the 4-hour photocatalytic process (top). The XRD measurements were performed for the platelets cast on a single-crystalline Si sample holder. (f) Comparison of the Bi 4f XPS spectra of the as-prepared $SrTiO_3/Bi_4Ti_3O_{12}$ platelets and after the 4-hour photocatalytic H_2 evolution (post HER).

$SrTiO_3$ nanoplatelets immediately lost their colouring. On the contrary, the heterostructure's intense black color remained stable and this was also confirmed by UV-VIS spectroscopy (Fig. S13b). SEM-secondary electron (SEM-SE) micrographs taken after a 4-hour photocatalytic process revealed no apparent morphological degradation in either sample type (Fig. 6a-d and Fig. 7a, b). According to XRD analysis, the photocatalytic process did not induce any structural changes to $SrTiO_3$. However, the disappearance of the $Bi_4Ti_3O_{12}$ diffraction lines from the XRD pattern indicated a chemical transformation of the $Bi_4Ti_3O_{12}$ component within the heterostructure (Fig. 6e). Post-reaction ex-situ XPS analysis of the active rough-surfaced heterostructures revealed a significant increase in metallic Bi^0 (Fig. 6f), while Ti remained in the Ti^{4+} state (Fig. S14a).

The light-induced structural changes of the $Bi_4Ti_3O_{12}$ part of the heterostructures were further investigated by STEM (Fig. 8). The thinned-to-electron transparency platelets were analysed in the edge-on orientation. HAADF-STEM disclosed severe deterioration of the $Bi_4Ti_3O_{12}$ layered structure as shown by comparing $SrTiO_3$-$Bi_4Ti_3O_{12}$ platelets before (Fig. 8a) and after H_2 evolution (Fig. 8b). Magnified images (Fig. 8c) show that previously single-crystal $Bi_4Ti_3O_{12}$ composed of $[Bi_2O_2]^{2+}$ layers and $[Bi_2Ti_3O_{10}]^{2-}$ blocks, was replaced by the newly formed well-aligned crystallites, surrounded by the amorphous phase, whereas the $SrTiO_3$ platelets, epitaxially grown on both surfaces, appear to remain fairly intact. A heterostructural platelet with $SrTiO_3$ in [100] zone axis (see FFT in Fig. 8d) was investigated in more detail. In this orientation, the $Bi_4Ti_3O_{12}$ would be oriented in [110] zone axis, with basal planes of $Bi_4Ti_3O_{12}$ parallel to the (010) planes of $SrTiO_3$. A combination of EDS analysis, HR STEM and Fast Fourier Transform (FFT) analysis revealed that the crystallites are metallic Bi° with rhombohedral crystal structure. The Bi particles crystallize as elongated grains with diameter of around 5–10 nm and lengths of tens of nanometres. Structural analysis of the Bi particles has shown that they follow two main orientations (Fig. 8e). In the first orientation, the (003) lattice planes are parallel to the basal planes of the (original) $Bi_4Ti_3O_{12}$, whereas in the second orientation, the (012) planes of Bi are parallel to the same set of planes. We assume that onset of recrystallization on the $[Bi_2O_2]^{2+}$ sections of the $Bi_4Ti_3O_{12}$ structure composed of double layer of Bi atoms would lead to formation of (003) lattice planes of Bi, whereas onset of recrystallization in the pseudoperovskite block would preferentially lead to the crystallization of (012) lattice planes of Bi and different orientation of the Bi grains (Fig. 8e) where the (012) planes of Bi are parallel to the basal planes of the original $Bi_4Ti_3O_{12}$.

The chemically bonded epitaxial heterostructures are generally more stable than physically bonded ones [5,30]. The particular instability of the $Bi_4Ti_3O_{12}$ inner part of the heterostructures is associated with the well-documented ease of reducing bismuth-based compounds into metallic Bi° by light and/or mild reductive atmosphere. Numerous studies have demonstrated the formation of Bi° nanostructures through photoreduction, solvothermal/hydrothermal treatment or by chemical reduction of bismuth-containing salts, oxides, oxychlorides, etc. (Table S4, Table S5) [31]. In our heterostructures, Bi° forms internally from $Bi_4Ti_3O_{12}$ and is shielded above and below by $SrTiO_3$. Only the laeral parts were directly exposed to light and liquid. BSE imaging (Figs. 6 c, d) revealed decreasing central brightness with prolongation of

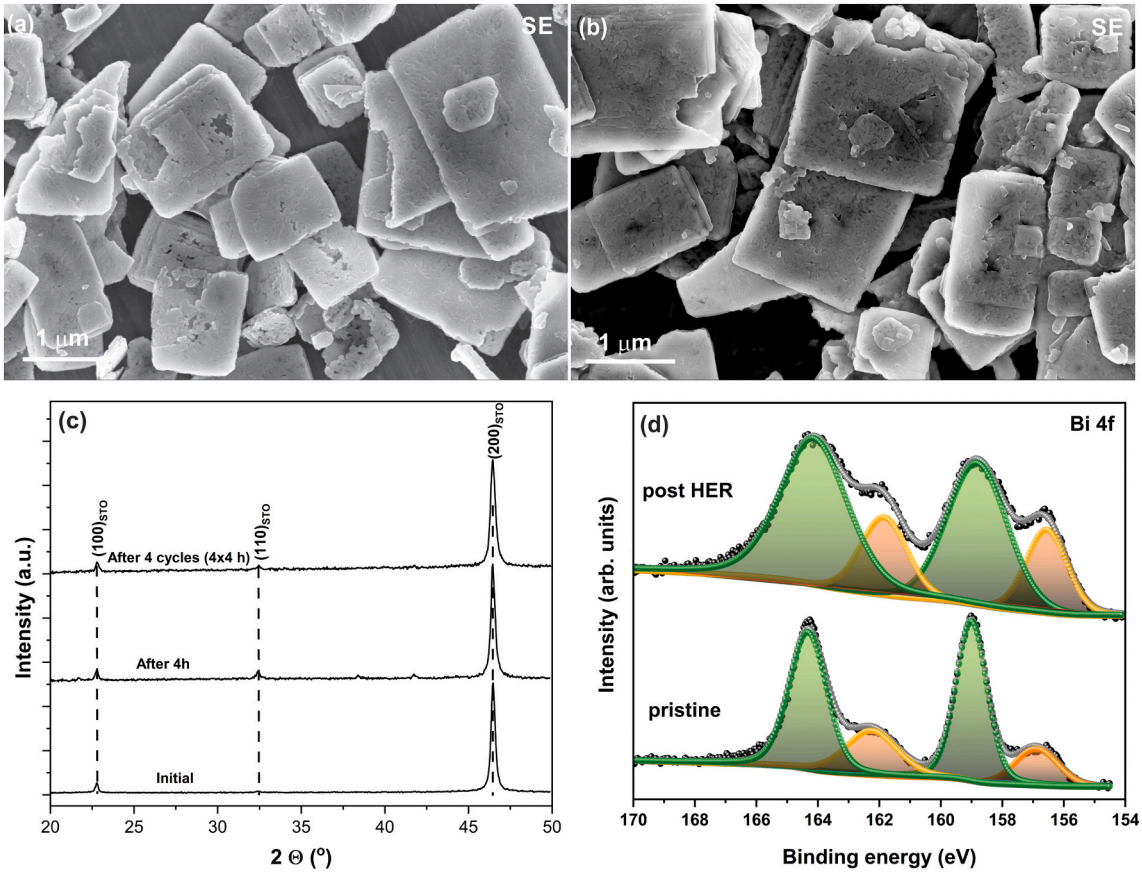

Fig. 7. (a, b) Secondary electron (SE) SEM micrographs of (a) as-prepared $SrTiO_3$ platelets (Sample H3) and (b) after 4 cycles of 4-hour photocatalytic process. (c) Comparison of the XRD pattern of the as-prepared $SrTiO_3$ platelets (bottom curve) with those after the 4-hour photocatalytic process (middle) and after 4 cycles of the 4-hour photocatalytic process (top). The XRD measurements were performed for the platelets cast on a single-crystalline Si sample holder. (d) Comparison of the Bi 4f XPS spectrum of the pristine $SrTiO_3$ platelets and after 4-hour photocatalytic H_2 evolution reaction (post HER).

the photocatalytic process, which implies gradual delamination of the forming Bi° core from the $SrTiO_3$ part. Considering that the progressive $Bi_4Ti_3O_{12}$ degradation did not cause any apparent interferences in photocatalytic performance across the four tested cycles (Fig. 5b), the exposed rough $SrTiO_3$ surface is most likely the main active region.

Such rough surface and porous morphological characteristics certainly play an important role in the photocatalytic activity, but it is unlikely to be the only determining factor. For example, in similar porous TiO_2 systems, other parameters, such as crystallinity, phase composition, fluorine in the TiO_2 lattice, Cu_2O co-catalysts, etc., also influence their photocatalytic performance [25–28]. Nonetheless, the formation of porous nanostructures could be an important design strategy for the enhancement of photocatalytic efficiency in TiO_2 and $SrTiO_3$ nanostructures.

The slight darkening of the active rough-surface $SrTiO_3$ nanoplatelets under light illumination (see Fig. S13 c and d) indicates light-induced reduction changes in these platelets. Ex-situ XPS analysis after the photocatalytic process confirmed that the greyish color of $SrTiO_3$ originated from an increase in Bi°, rather than from the reduction of Ti^{4+} to Ti^{3+} (see Fig. 7d and Fig. S14b). Since the morphology and spatial distribution of bismuth determine its role in the photocatalytic process, scanning transmission electron microscopy (STEM) was employed to examine the distribution of Bi within the rough $SrTiO_3$ platelets.

Fig. 9a shows a platelet that has been completely transformed into $SrTiO_3$ according to Procedure 2, resulting in platelets with a high surface area (rough surface). EDS mapping of a small area of this platelet reveals nanosized bismuth-enriched regions (Fig. 9c). Their distribution across the platelet is fairly homogeneous, and they are well-separated from each other. High-resolution HAADF-STEM analysis (Figs. 9d, e) shows that Bi is present in clusters up to 10 nm in size, featuring aggregated Bi in the core and well-separated single Bi atoms at the periphery. Additionally, many Bi single atoms can be observed on the surface of the $SrTiO_3$ platelet as bright dots due to the high atomic number of Bi (Z = 83).

Considering that XPS analysis of the as-prepared rough $SrTiO_3$ nanoplatelets indicates the dominance of Bi^{3+} species, these isolated Bi atoms (including those in the clusters) arise from trapped Bi^{3+} ions coordinated with the oxygen anions of the perovskite lattice. The possibility that the cluster core also consists of trapped Bi_2O_3 nanoparticles cannot be excluded. For clarity and consistency, these bismuth-containing nanospecies are henceforth denoted as Bi single atoms/clusters. A comparison of active and non-active $SrTiO_3$ platelets in terms of EDS composition showed very similar amounts of bismuth (0.5 at. %) residues. Nevertheless, rough-surfaced $SrTiO_3$ platelets offer more accessible active sites, with a greater fraction of Bi exposed at the surface, in contrast to the smoother platelets where Bi residues are more likely to be embedded within solid $SrTiO_3$. Therefore, the improved activity of the platelets with a high surface area can be attributed to the increased surface availability of Bi single atoms/clusters, which are more likely to participate in the photocatalytic process (Figs. 9e, f).

These findings align well with previous reports, confirming the enhancement of the photocatalytic performances of semiconductors by their decoration with Bi°/Bi_2O_3 nanodots or Bi_2O_3 nanostructures (e.g. NO removal over Bi°/BiOCl [32], Bi°/g-C_3N_4 [33] and Bi°/TiO_2 (P25) [34], CO_2 reduction by Bi°/Bi_2O_3/TiO_2 [35] and by Bi^{3+}/TiO_2 [36], phenol degradation by Bi°/BiOI-Bi_2O_3 [37] and NH_3 synthesis by Bi/$BiFeO_3$ [38], Bi/$Bi_2Sn_2O_7$ [39] and Bi/$BaTiO_3$ [40] (Table S4). Notably, the photocatalytic reduction of CO_2 to CO (E = - 0.53 V vs NHE at pH =

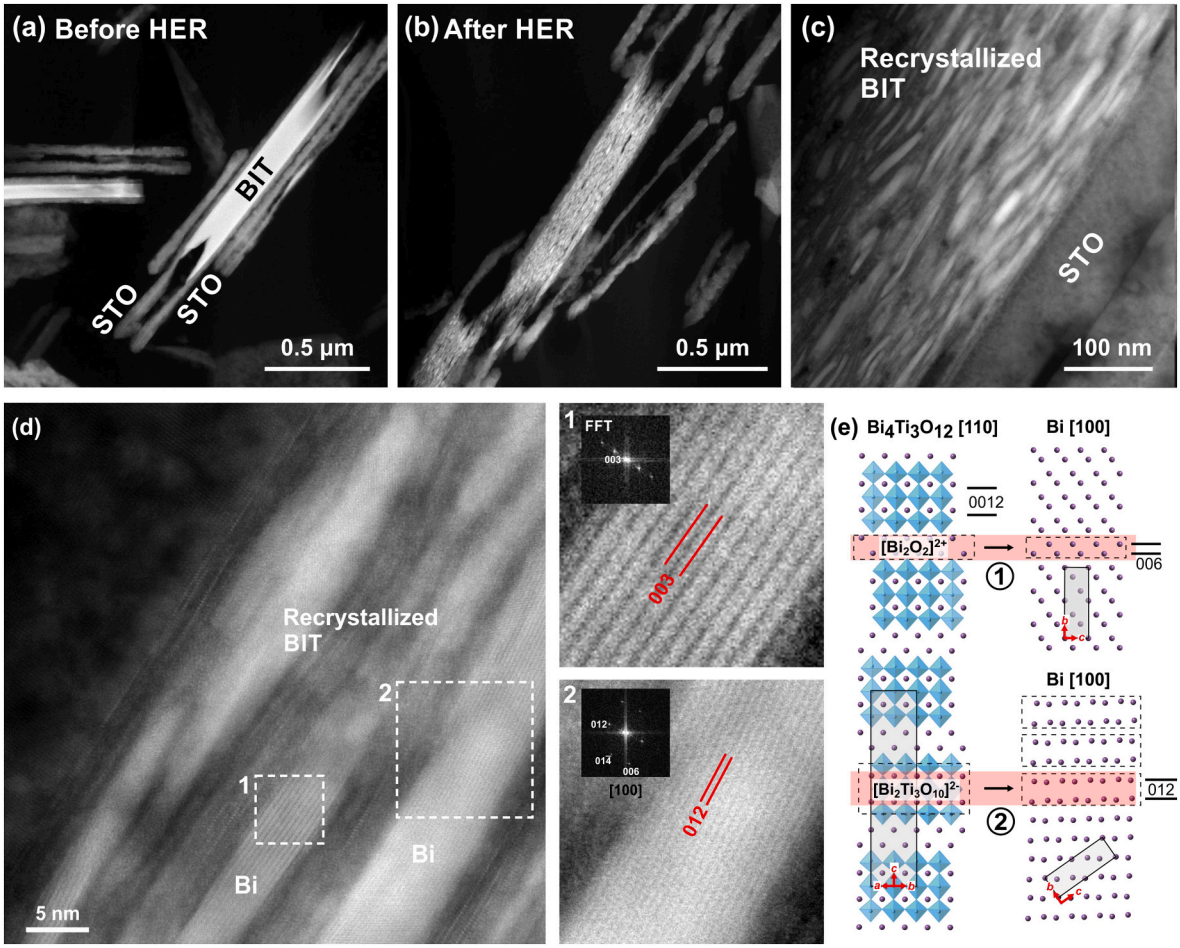

Fig. 8. HAADF-STEM images of edge-on oriented $SrTiO_3/Bi_4Ti_3O_{12}$ (STO/BIT) platelets: (a) as prepared and (b-d) after 4-hour photocatalytic H_2 evolution reaction. (c) Recrystallisation of single-crystal $Bi_4Ti_3O_{12}$ to a composite material consisting of crystalline nanoparticles embedded in an amorphous matrix. (d) The crystalline grains are metallic Bi° with two different orientations (1 and 2). (e) Schematic presentation of the transformation of oriented $Bi_4Ti_3O_{12}$ to metallic Bi° in two orientations.

7) requires even more negative potential than photocatalytic H_2 evolution ($2H^+ + 2e^- \Rightarrow H_2$ (E = -0.41 V vs NHE at pH = 7) [41]. Bi° or Bi_2O_3 as a cocatalyst has also been reported to enhance photocatalytic H_2 evolution of several semiconductors, including TiO_2 [42–45], g-C_3N_4 [42,46], CdS [42], $Bi_2O_2CO_2$ [47], BiOCl [48], $ZnIn_2S4$ [49] [50], N-doped porous C with Bi-MOF [51] and various direct Z/S-Scheme system such as Bi_5O_7I/Sn_3O_4 [52], $Bi_2MoO_6/ZnIn_2S_4$ [53], $Bi_2WO_6/H\text{-}TiO_2$ [54]. It was confirmed in several systems (Table S5) that the optimal amount of Bi, leading to remarkable improvement of the H_2 generation rates (14-times -108 times), is typically small in the range 0.25 % - 1 %. For example, Gao et al. observed a 106-times improvement of the H_2-evolution rate by in-situ photo-deposited 1 wt% (nominal concentration) of Bi° on TiO_2 [42]. The actual content of bismuth determined by XPS was 0.2 at.%, which is comparable to the bismuth contents in our $SrTiO_3$ platelets. Similarly, Xu et al. [43],Reddy et al. [44] and Du et al. [45] reported 73-times, 5-times and 40.8-times improvement of H_2 evolution rates for different TiO_2 nanostructures loaded with Bi_2O_3 in the amount of 0.89 mol% Bi_2O_3, 0.5 wt% Bi, and 0.23 mol% Bi, respectively. The photocatalytic performances of as-prepared $SrTiO_3$ (1908 μmol g^{-1} h^{-1}), $SrTiO_3/Bi_4Ti_3O_{12}$ nanoplatelets (2950 μmol g^{-1} h^{-1}), and $SrTiO_3$ nanoplatelets additionally loaded with Pt (3781 μmol g^{-1} h^{-1}, Fig. S15) are comparable to other similar well-performing photocatalysts (Table S5). Several systems show much lower activity below 1000 μmol g^{-1} h^{-1}, only N-doped porous carbon loaded with Bi nanoclusters obtained from Bi-MOF, stands out with a superior performance of 12,800 μmol g^{-1} h^{-1} . The results, summarised in Table S5, highlight the interest in designing photocatalysts by integrating non-noble metal bismuth with various semiconductors and studying their photocatalytic mechanisms and performances. Notably, since the H_2 evolution photocatalytic tests listed in Table S5 were performed in water/alcohol solutions, the Bi°/semiconductor systems demonstrate potential for H_2 evolution through simultaneous decomposition of organic compounds in the processes of so-called dual-functional photocatalysis [55,56] and photoreforming [57].

To obtain insight into the photocatalytic mechanism and charge transfer process in the studied $SrTiO_3$ nanoplatelets, photoelectrochemical (PEC) measurements and electrochemical impedance spectroscopy (EIS) were performed (Fig. 10). The heterostructural $SrTiO_3/Bi_4Ti_3O_{12}$ platelets were excluded from these studies because of their structural instability. Degradation of the internal $Bi_4Ti_3O_{12}$ component under illumination might prevent reliable interpretation of the spectrochemical results. Linear sweep voltammetry (Fig. 10a) shows that all three $SrTiO_3$ samples are active for H_2 evolution but the catalytic rate of the sample C3 is much lower compared to samples C4 and H3. The trend in PEC performance is in line with the H_2 evolution rate observed in photocatalytic evaluation. Nyquist plots (Fig. 10 b) obtained from the EIS measurements were fit with an equivalent electric circuit comprising two resistors, representing the solution resistance (R_{sol}) and interfacial charge-transfer resistance (R_{ct}) (Fig. S16 and Table S7). Sample H3 shows the lowest R_{ct} values, suggesting faster interfacial kinetics at the catalyst/electrolyte interface, which also explains its higher H_2 evolution rate. The circuit also contains two capacitors (C_s and

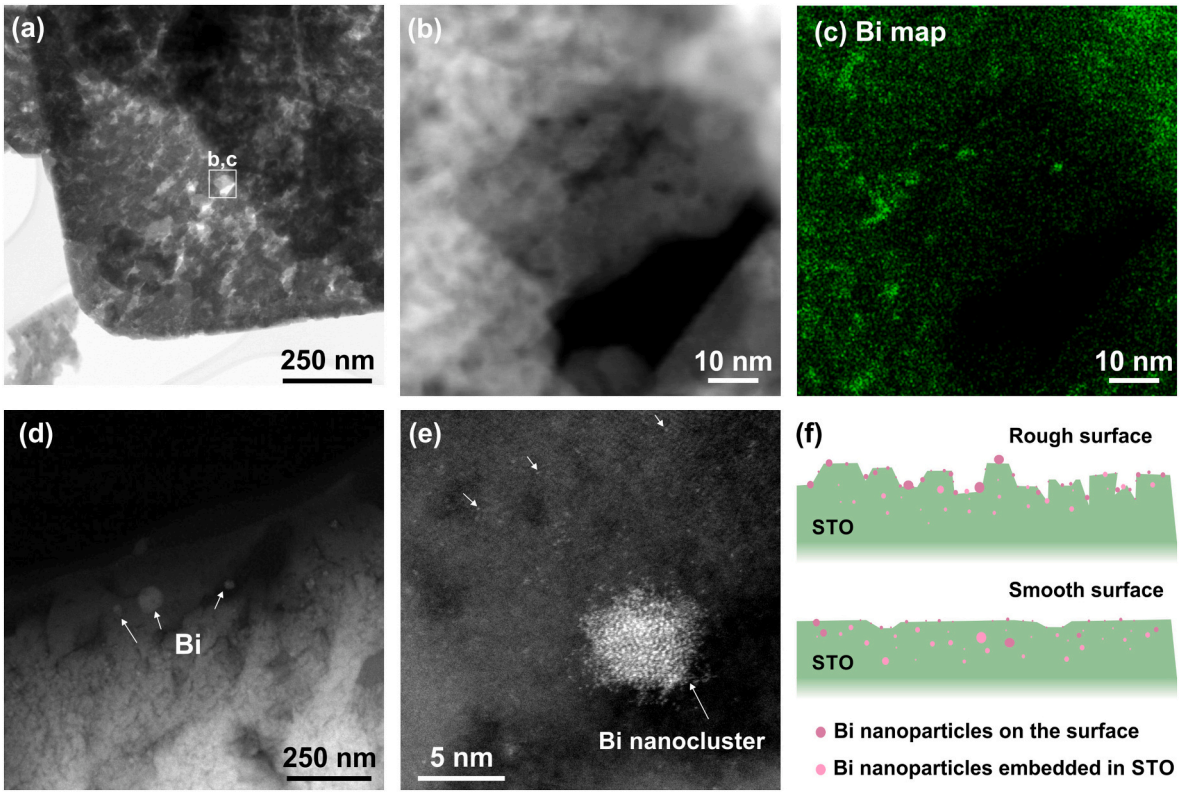

Fig. 9. (a) Bright field (BF) STEM top view of the part of the $SrTiO_3$ (STO) nanoplatelets and (b) Dark field (DF) STEM of the denoted magnified area in the interior part of the STO platelet, containing nano-sized bismuth species as shown by (c) EDS mapping. (d, e) High-resolution HAADF-STEM image showing Bi in the form of a nanocluster with around 7 nm in diameter and many individual Bi atoms (some indicated by arrows) on the surface of the platelet. (f) Schematic presentation of the Bi single atoms and clusters on a rough and smooth surface of $SrTiO_3$ nanoplatelets, showing that many more Bi single atoms and clusters may reside on the surface of the rough platelets and are thus available for the photocatalytic reaction.

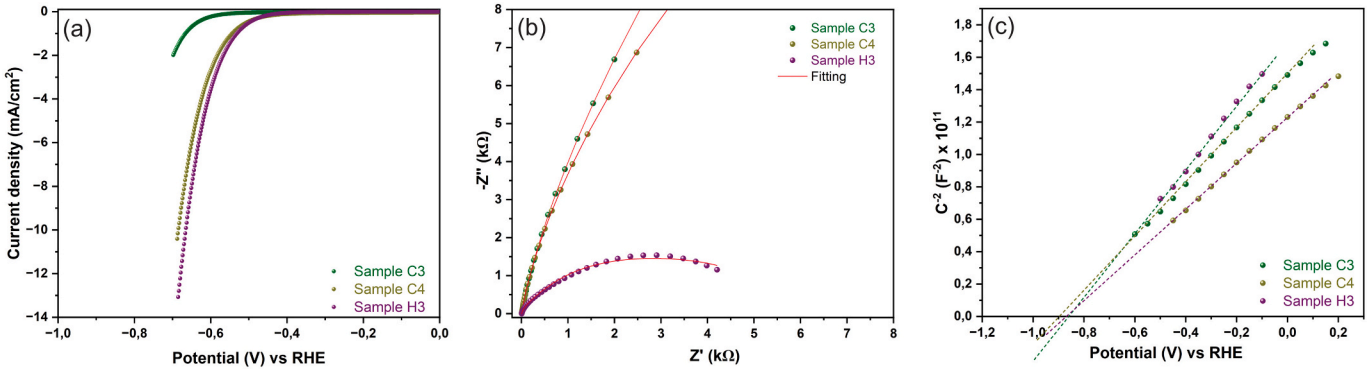

Fig. 10. (a) Cathodic linear polarization curves, (b) Nyquist plots obtained from EIS measurements and (c) Mott-Schottky plots measured at 1000 Hz for $SrTiO_3$ nanoplatelets (samples C3, C4 and H3) in 1 M KOH.

C_{dl}), corresponding to the capacitance due to the semiconducting catalyst (C_s) and the electric double layer formed at the catalyst/electrolyte interface (C_{dl}). It is notable that all the three catalysts show almost similar values for C_s, which is expected due to the same catalyst material. However, the value for C_{dl} is almost 12 times higher in H3 compared to C3 and C4. C_{dl} originates due to the interfacial interaction between the catalyst surface and the electrolyte, and a higher value is attributed to the high surface area of H3, which offers better percolation of the electrolyte into the catalyst surface, benefiting the surface redox activity. Mott-Schottky analysis (Fig. 10 c) revealed positive slopes for the $SrTiO_3$ platelets, confirming their n-type behaviour. The X-axis intercept of the extrapolated data gives flat-band potentials of −0.85 V, −0.89 V and −0.87 V vs. RHE for samples C3, C4 and H3, matching well with the reported E_{CB} levels for $SrTiO_3$ (−0.80 V - −0.81 V) [7,58].

Band structure analysis is a prerequisite for understanding the photocatalytic mechanism. Considering that the measured optical band gap of $SrTiO_3$ is 3.26 eV, and its reported conduction band potential (E_{CB}) is −0.8 V, the valence band position is thus 2.46 V. The photoreduction of Bi^{3+} to Bi° on the $SrTiO_3$ is thermodynamically feasible, as it is inferred from the more negative E_{CB} of $SrTiO_3$ compared to the reduction potential of Bi^{3+}/Bi° (0.308 V) [59]. This reaction is also supported by empirical evidence of Bi° formation from Bi_2O_3 on the semiconductors with similarly negative E_{CB} (Tables S4 and S5).

The most plausible photocatalytic mechanism of the $SrTiO_3$ nanoplatelets with surface-trapped Bi single atoms, or clusters (Fig. S17), is similar to those reported for other n-type semiconductors decorated

with bismuth-based nanostructures [42,43]. Upon illumination with light of energy exceeding the band gap of $SrTiO_3$ (3.26 eV), electrons are excited from the valence band (E_{VB} = 2.46 V) to the conduction band (E_{CB} = −0.8 V), leaving behind holes in the valence band. The relatively less negative reduction potential of Bi^{3+}/Bi°(0.308 eV) makes the reduction of Bi^{3+} into Bi° by the conduction band electrons of $SrTiO_3$ thermodynamically favourable. As a result, the photogenerated electrons reduce surface-anchored Bi^{3+} into metallic Bi° (Fig. S17). Moreover, the Fermi level (E_f) of n-type $SrTiO_3$ (typically 0.1 eV–0.3 eV below E_{CB} minimum) is more negative than the Fermi level (E_f) of metallic Bi° (E_f = −0.17 eV) [60]. This difference drives the electron transfer from $SrTiO_3$ to Bi° till the Fermi levels equalise (Fig. S17). The resulting apparent equilibrium Fermi level (E_f*) is more negative than that of metallic Bi° and thus sufficient to enable H_2 production. Additionally, the formation of the Schottky barrier at the Bi°-$SrTiO_3$ interface leads to electron accumulation in the Bi° sites, which then act as active centres for H_2 generation. Meanwhile, the photo-generated holes are expected to react with methanol, which acts as the hole scavenger.

4. Conclusions

This study enhances our understanding of the hydrothermal transformation of $Bi_4Ti_3O_{12}$ Aurivillius phase platelets into 2D $SrTiO_3$ nanostructures, providing a pathway for rational control of $SrTiO_3$ surface roughness and functional properties.

By systematically varying the experimental parameters, such as the size of the $Bi_4Ti_3O_{12}$ template nanoplatelets, strontium excess (Sr/Ti molar ratios = 12–15), and the temperature of the initial NaOH solution, we successfully synthesised both heterostructural $SrTiO_3/Bi_4Ti_3O_{12}$ and pure $SrTiO_3$ nanoplatelets with varying surface roughness and exhibiting BET surface areas of 6 m^2/g - 64 m^2/g.

Smaller template sizes, higher strontium excess, and pre-treatment of initial platelets with warm NaOH promoted the formation of rougher, high-surface-area nanoplatelets. Photocatalytic hydrogen evolution showed higher correlation with surface morphology than with composition: smooth nanoplatelets (BET 12 m^2/g) exhibited low activity (3 $\mu mol \cdot g^{-1} \cdot h^{-1}$-69 $\mu mol \cdot g^{-1} \cdot h^{-1}$), while the rougher structures (53 m^2/g – 64 m^2/g) showed much higher H_2 evolution rates (1908 $\mu mol \cdot g^{-1} \cdot h^{-1}$- 2950 $\mu mol \cdot g^{-1} \cdot h^{-1}$) in neutral water/methanol solutions. Under light illumination, the $SrTiO_3$ part retained its chemical, structural, and morphological integrity, while the internal $Bi_4Ti_3O_{12}$ part of the heterostructures transformed into metallic Bi° and an amorphous phase, without impairing photocatalytic performance under tested conditions. This suggests that the heterojunction plays a minor role, highlighting $SrTiO_3$ as the main active component.

STEM analysis revealed a uniform distribution of Bi single atoms and clusters (~0.5 at. %) embedded within the rough $SrTiO_3$ surface. The metallic Bi°, formed mainly by in situ photoreduction of Bi^{3+} species, functions as a non-noble metal co-catalyst. Literature reports support the idea, that Bi°-containing systems are more suited for photo-redox processes, where H_2 evolution is coupled with oxidation of organics rather than for overall water splitting. This suggests that future studies should focus on dual-functional research, targeting reactions that yield value-added products or degrade pollutants in addition to producing H_2.

Finally, the demonstrated transformation from $Bi_4Ti_3O_{12}$ to 2D $SrTiO_3$ offers a template for engineering of other $Bi_4Ti_3O_{12}$-derived 2D $ATiO_3$ perovskites (A = Ba, Ca, Sr, $Ba_{1-x}Sr_x$) with high application potential in piezocatalysis, dual-functional photocatalysis, pyro catalysis, piezo-photocatalysis, photo-pyro catalysis, etc. Each system presents unique opportunities and challenges for controlling the structure-function relationship to achieve optimised performance.

CRediT authorship contribution statement

Marjeta Maček Kržmanc: Writing – review & editing, Writing – original draft, Methodology, Investigation, Funding acquisition, Formal analysis, Data curation, Conceptualization. **Nina Daneu:** Writing – review & editing, Methodology, Investigation, Funding acquisition, Formal analysis, Data curation. **Khaja Mohaideen Kamal:** Writing – review & editing, Methodology, Investigation, Formal analysis, Data curation, Conceptualization. **Blaž Likozar:** Writing – review & editing. **Alja Čontala:** Writing – review & editing, Investigation. **Matjaž Spreitzer:** Writing – review & editing, Methodology. **Jeffrey C.S. Wu:** Writing – review & editing, Funding acquisition, Formal analysis, Conceptualization. **Suraj Gupta:** Writing – review & editing, Methodology, Investigation, Formal analysis, Data curation, Conceptualization.

Declaration of competing interest

The authors declare that they have no known competing financial interests or personal relationships that could have appeared to influence the work reported in this paper.

Acknowledgements

This work was supported by the Ministry of Higher Education, Science and Innovation of Slovenia and National Science and Technology Council (NSTC), Taiwan (M-ERA.NET project HetCat (No. 10382, Contract No. C3360-23-252003 (Slovenia), grant numbers NSTC 114-2923-E-002-003 (Taiwan)), Slovenian Research and Innovation Agency (ARIS) (Research program (P2–0091) and research projects (No. J1-3025, J2-50055)), HORIZON-TMA-MSCA-SE action (H-GREEN project »Innovative Functional Oxide Materials for Green Hydrogen Energy Production), European climate, infrastructure and environment executive agency (CINEA) (grant agreement No. 101118129, Project: PHOTOSINT) and the European innovation council and SMES executive agency (EISMEA) (grant agreement No. 101046836, Project: CATART).

The authors would also like to thank Blaž Antonin, Rok Kozamernik, Lan Čuček Meršol, Mihael Turkovic, and Zoja Vučić for their help in the synthesis procedures, Medeja Gec for preparing the samples for the TEM examinations and Silvo Zupančič for BET specific surface area measurements.

Appendix A. Supplementary data

Supplementary data to this article can be found online at https://doi.org/10.1016/j.cej.2025.171758.

Data availability

Data will be made available on request.

References

[1] H. Song, S. Luo, H. Huang, B. Deng, J. Ye, Solar-driven hydrogen production: recent advances, challenges, and future perspectives, ACS Energy Lett. 7 (2022) 1043–1065, https://doi.org/10.1021/acsenergylett.1c02591.

[2] T. Takata, J. Jiang, Y. Sakata, M. Nakabayashi, N. Shibata, V. Nandal, K. Seki, T. Hisatomi, K. Domen, Photocatalytic water splitting with a quantum efficiency of almost unity, Nature 581 (2020) 411–414, https://doi.org/10.1038/s41586-020-2278-9.

[3] H. Nishiyama, T. Yamada, M. Nakabayashi, Y. Maehara, M. Yamaguchi, Y. Kuromiya, Y. Nagatsuma, H. Tokudome, S. Akiyama, T. Watanabe, R. Narushima, S. Okunaka, N. Shibata, T. Takata, T. Hisatomi, K. Domen, Photocatalytic solar hydrogen production from water on a 100-m2 scale, Nature 598 (2021) 304–307, https://doi.org/10.1038/s41586-021-03907-3.

[4] A. Hezam, T. Peppel, J. Strunk, Pathways towards a systematic development of Z-scheme photocatalysts for CO2 reduction, Curr. Opin. Green Sustain. Chem. 41 (2023) 100789, https://doi.org/10.1016/j.cogsc.2023.100789.

[5] L. Wang, K. Xu, W. Cui, D. Lv, L. Wang, L. Ren, X. Xu, F. Dong, S.X. Dou, W. Hao, Y. Du, Monolayer epitaxial heterostructures for selective visible-light-driven photocatalytic NO oxidation, Adv. Funct. Mater. 29 (2019) 1808084, https://doi.org/10.1002/adfm.201808084.

[6] A. Čontala, N. Daneu, S. Gupta, M. Spreitzer, A. Meden, M. Maček Kržmanc, Hydrothermal topotactic epitaxy of SrTiO3 on Bi4Ti3O12 nanoplatelets: understanding the interplay of lattice mismatch and supersaturation, Nanoscale Adv. 5 (2023) 3005–3017, https://doi.org/10.1039/d2na00741j.

[7] M. Maček Kržmanc, N. Daneu, A. Čontala, S. Santra, K.M. Kamal, B. Likozar, M. Spreitzer, SrTiO3/Bi4Ti3O12 nanoheterostructural platelets synthesized by topotactic epitaxy as effective noble-metal-free photocatalysts for pH-neutral hydrogen evolution, ACS Appl. Mater. Interfaces 13 (2021) 370–381, https://doi.org/10.1021/acsami.0c16253.
[8] V. Kalyani, B.S. Vasile, A. Ianculescu, A. Testino, A. Carino, M.T. Buscaglia, V. Buscaglia, P. Nanni, Hydrothermal synthesis of SrTiO3: role of interfaces, Cryst. Growth Des. 15 (2015) 5712–5725, https://doi.org/10.1021/acs.cgd.5b00770.
[9] V. Kalyani, B.S. Vasile, A. Ianculescu, M.T. Buscaglia, V. Buscaglia, P. Nanni, Hydrothermal synthesis of SrTiO 3 mesocrystals: single crystal to mesocrystal transformation induced by topochemical reactions, Cryst. Growth Des. 12 (2012) 4450–4456, https://doi.org/10.1021/cg300614f.
[10] S.F. Poterala, Y. Chang, T. Clark, R.J. Meyer, G.L. Messinge, Mechanistic interpretation of the aurivillius to perovskite topochemical microcrystal conversion process, Chem. Mater. 22 (2010) 2061–2068, https://doi.org/10.1021/cm903315u.
[11] M.M. Kržmanc, B. Jančar, H. Uršič, M. Tramšek, D. Suvorov, Tailoring the shape, size, crystal structure, and preferential growth orientation of BaTiO3 Plates synthesized through a topochemical conversion process, Cryst. Growth Des. 17 (2017) 3210–3220, https://doi.org/10.1021/acs.cgd.7b00164.
[12] M.M. Kržmanc, H. Uršič, A. Meden, R.C. Korošec, D. Suvorov, Ba1-xSrxTiO3 plates: synthesis through topochemical conversion, piezoelectric and ferroelectric characteristics, Ceram. Int. 44 (2018) 21406–21414, https://doi.org/10.1016/j.ceramint.2018.08.198.
[13] J. Wu, Y. Chang, W. Lv, G. Jiang, Y. Sun, Y. Liu, S. Zhang, B. Yang, W. Cao, Topochemical transformation of single crystalline SrTiO3 microplatelets from Bi4Ti3O12 precursors and their orientation-dependent surface piezoelectricity, CrystEngComm 20 (2018) 3084–3095, https://doi.org/10.1039/c8ce00473k.
[14] Y. Chang, H. Ning, J. Wu, S. Zhang, T. Lü, B. Yang, W. Cao, Formation mechanism of (001) oriented perovskite SrTiO3 microplatelets synthesized by topochemical microcrystal conversion, Inorg. Chem. 53 (2014) 11060–11067, https://doi.org/10.1021/ic501604c.
[15] J. Wang, W. Liu, D. Zhong, Y. Ma, Q. Ma, Z. Wang, J. Pan, Fabrication of bismuth titanate nanosheets with tunable crystal facets for photocatalytic degradation of antibiotic, J. Mater. Sci. 54 (2019) 13740–13752, https://doi.org/10.1007/s10853-019-03882-1.
[16] M. Škarabot, M. Maček Kržmanc, L. Rupnik, G. Lahajnar, D. Suvorov, I. Muševič, Electric-field-induced reorientation of ferroelectric micro- and nano-platelets in the nematic liquid crystal, Liq. Cryst. 48 (2021) 385–394, https://doi.org/10.1080/02678292.2020.1785026.
[17] D. Makovec, N. Križaj, A. Meden, G. Dražić, H. Uršič, R. Kostanjšek, M. Šala, S. Gyergyek, Ferroelectric bismuth-titanate nanoplatelets and nanowires with a new crystal structure, Nanoscale 14 (2022) 3537–3544, https://doi.org/10.1039/d2nr00307d.
[18] H. He, J. Yin, Y. Li, Y. Zhang, H. Qiu, J. Xu, T. Xu, C. Wang, Size controllable synthesis of single-crystal ferroelectric Bi4Ti3O12 nanosheet dominated with {001} facets toward enhanced visible-light-driven photocatalytic activities, Appl. Catal. Environ. 156–157 (2014) 35–43, https://doi.org/10.1016/j.apcatb.2014.03.003.
[19] A. Čontala, M.M. Kržmanc, D. Suvorov, Plate-like Bi4Ti3O12 particles and their topochemical conversion to SrTiO3 under hydrothermal conditions, Acta Chim. Slov. 65 (2018) 630–637, https://doi.org/10.17344/acsi.2018.4286.
[20] Q. Tang, J. Wu, D. Kim, C. Franco, A. Terzopoulou, A. Veciana, J. Puigmartí-Luis, X. Chen, B.J. Nelson, S. Pané, Enhanced piezocatalytic performance of $BaTiO_3$ nanosheets with highly exposed {001} facets, Adv. Funct. Mater. (2022) 2202180, https://doi.org/10.1002/adfm.202202180.
[21] K. Ke, J. Wu, Z. Kang, E. Lin, N. Qin, D. Bao, Ultrathin Ba0.75Sr0.25TiO3 nanosheets with highly exposed {001} polar facets for high-performance piezocatalytic application, Nanoscale 16 (2024) 15652–15662, https://doi.org/10.1039/d4nr02203c.
[22] M. Vukomanović, L. Gazvoda, M. Kurtjak, M. Maček-kržmanc, M. Spreitzer, Q. Tang, J. Wu, H. Ye, X. Chen, M. Mattera, J. Puigmartí-luis, S.V. Pane, Filler-enhanced piezoelectricity of poly- L -lactide and its use as a functional ultrasound-activated biomaterial, Small (2023) 2301981, https://doi.org/10.1002/smll.202301981.
[23] P. Makuła, M. Pacia, W. Macyk, How to correctly determine the band gap energy of modified semiconductor photocatalysts based on UV-Vis spectra, J. Phys. Chem. Lett. 9 (2018) 6814–6817, https://doi.org/10.1021/acs.jpclett.8b02892.
[24] Z.J. Gong, C.C. Chien, S. Mudhulu, J.C.S. Wu, N. Daneu, M.M. Kržmanc, W.Y. Yu, SrTiO3 catalysts prepared from topochemical conversion of Bi4Ti3O12 nanoplatelets: surface characterizations and interactions with isopropanol, J. Catal. 416 (2022) 222–232, https://doi.org/10.1016/j.jcat.2022.11.001.
[25] L. Ren, Y. Li, J. Hou, X. Zhao, C. Pan, Preparation and enhanced photocatalytic activity of TiO2 nanocrystals with internal pores, ACS Appl. Mater. Interfaces 6 (2014) 1608–1615, https://doi.org/10.1021/am404457u.
[26] L. Ren, Y. Li, J. Hou, T. Wang, Y. Yang, X. Zhao, Fabrication and cavity-size-dependent photocatalytic property of TiO2 hollow nanoparticles with tunable cavity size, Mater. Res. Bull. 126 (2020) 110744, https://doi.org/10.1016/j.materresbull.2019.110744.
[27] D. Praveen Kumar, N. Lakshmana Reddy, M. Karthikeyan, N. Chinnaiah, V. Bramhaiah, V. Durga Kumari, M.V. Shankar, Synergistic effect of nanocavities in anatase TiO2 nanobelts for photocatalytic degradation of methyl orange dye in aqueous solution, J. Colloid Interface Sci. 477 (2016) 201–208, https://doi.org/10.1016/j.jcis.2016.05.014.
[28] D. Praveen Kumar, N. Lakshmana Reddy, M. Mamatha Kumari, B. Srinivas, V. Durga Kumari, B. Sreedhar, V. Roddatis, O. Bondarchuk, M. Karthik, B. Neppolian, M.V. Shankar, Cu2O-sensitized TiO2 nanorods with nanocavities for highly efficient photocatalytic hydrogen production under solar irradiation, Sol. Energy Mater. Sol. Cells 136 (2015) 157–166, https://doi.org/10.1016/j.solmat.2015.01.009.
[29] Q. Li, J. Zhang, B. Liu, M. Li, R. Liu, X. Li, H. Ma, S. Yu, L. Wang, Y. Zou, Z. Li, B. Zou, T. Cui, G. Zou, Synthesis of high-density nanocavities inside TiO2-B nanoribbons and their enhanced electrochemical lithium storage properties, Inorg. Chem. 47 (2008) 9870–9873, https://doi.org/10.1021/ic800758d.
[30] A. Šutka, M. Järvekülg, K.A. Gross, Photocatalytic nanoheterostructures and chemically bonded junctions made by solution-based approaches, Crit. Rev. Solid State Mater. Sci. 44 (2019) 239–263, https://doi.org/10.1080/10408436.2018.1485549.
[31] C. Yue, L. Zhu, Y. Qiu, Z. Du, J. Qiu, F. Liu, F. Wang, Recent advances of plasmonic elemental Bi based photocatalysts in environmental remediation and energy conversion, J. Clean. Prod. 392 (2023) 136017, https://doi.org/10.1016/j.jclepro.2023.136017.
[32] F. Dong, T. Xiong, S. Yan, H. Wang, Y. Sun, Y. Zhang, H. Huang, Z. Wu, Facets and defects cooperatively promote visible light plasmonic photocatalysis with Bi nanowires@BiOCl nanosheets, J. Catal. 344 (2016) 401–410, https://doi.org/10.1016/j.jcat.2016.10.005.
[33] G. Jiang, X. Li, M. Lan, T. Shen, X. Lv, F. Dong, S. Zhang, Monodisperse bismuth nanoparticles decorated graphitic carbon nitride: enhanced visible-light-response photocatalytic NO removal and reaction pathway, Appl. Catal. Environ. 205 (2017) 532–540, https://doi.org/10.1016/j.apcatb.2017.01.009.
[34] Z. Zhao, W. Zhang, X. Lv, Y. Sun, F. Dong, Y. Zhang, Noble metal-free Bi nanoparticles supported on TiO2 with plasmon-enhanced visible light photocatalytic air purification, Environ. Sci. Nano. 3 (2016) 1306–1317, https://doi.org/10.1039/c6en00341a.
[35] G. Yang, W. Miao, Z. Yuan, Z. Jiang, B. Huang, P. Wang, J. Chen, Bi quantum dots obtained via in situ photodeposition method as a new photocatalytic CO2 reduction cocatalyst instead of noble metals: borrowing redox conversion between Bi2O3 and Bi, Appl. Catal. Environ. 237 (2018) 302–308, https://doi.org/10.1016/j.apcatb.2018.06.018.
[36] X. Li, W. Bi, Z. Wang, W. Zhu, W. Chu, C. Wu, Y. Xie, Surface-adsorbed ions on TiO2 nanosheets for selective photocatalytic CO2 reduction, Nano Res. 11 (2018) 3362–3370, https://doi.org/10.1007/s12274-017-1933-4.
[37] Q. Wang, H. Wu, Q. Gao, D. Lin, Y. Fan, R. Duan, Y. Cong, Y. Zhang, Fabrication of visible-light-active Bi/BiOI-Bi 2 O 3 composite with enhanced photocatalytic activity, J. Colloid Interface Sci. 548 (2019) 255–264, https://doi.org/10.1016/j.jcis.2019.04.044.
[38] Z. Zeng, Y. Wang, X. Liu, B. He, J. Ding, Z. Li, P. Zhu, H. Wang, Y. Zhao, Y. Wang, In-situ precipitation enabled Bi / BiFeO 3 Schottky junction with an electronic tunnel for promoting photocatalytic ammonia synthesis, Appl. Catal. B Environ. Energy 378 (2025) 125596, https://doi.org/10.1016/j.apcatb.2025.125596.
[39] R. Wu, S. Gao, C. Jones, M. Sun, M. Guo, R. Tai, S. Chen, Q. Wang, Bi / BSO heterojunctions via vacancy engineering for efficient photocatalytic nitrogen fixation, Adv. Funct. Mater. 34 (2024) 2314051 (1–10), https://doi.org/10.1002/adfm.202314051.
[40] Z. Zeng, J. Wu, C. Xia, S. Yuan, X. Ren, L. Zhao, L. Zhuang, Y. He, Boosting photocatalytic efficiency with ohmic contact: a novel Bi / BaTiO 3 composite for nitrogen fixation and RhB degradation, J. Alloys Compd. 1010 (2025) 178312, https://doi.org/10.1016/j.jallcom.2024.178312.
[41] K. Li, B. Peng, T. Peng, Recent advances in heterogeneous photocatalytic CO2 conversion to solar fuels, ACS Catal. 6 (2016) 7485–7527, https://doi.org/10.1021/acscatal.6b02089.
[42] D. Gao, H. Yu, Y. Xu, Direct photoinduced synthesis and high H 2 -evolution performance of Bi-modified TiO 2 photocatalyst in a Bi(III)-EG complex system, Appl. Surf. Sci. 462 (2018) 623–632, https://doi.org/10.1016/j.apsusc.2018.08.061.
[43] D. Xu, Y. Hai, X. Zhang, S. Zhang, R. He, Bi 2 O 3 cocatalyst improving photocatalytic hydrogen evolution performance of TiO 2, Appl. Surf. Sci. 400 (2017) 530–536, https://doi.org/10.1016/j.apsusc.2016.12.171.
[44] N. Lakshmana Reddy, G. Krishna Reddy, K. Mahaboob Basha, P. Krishna Mounika, M.V. Shankar, Highly efficient hydrogen production using Bi2O3/TiO2 nanostructured photocatalysts under led light irradiation, Mater. Today Proc. 3 (2016) 1351–1358, https://doi.org/10.1016/j.matpr.2016.04.014.
[45] X. Du, J. Hu, J. Xie, Z. Lu, K. Wang, B. Liu, Y. Cao, Remarkable upgrade of hydrogen evolution activity up to 40.8 folds and mechanistic investigation of expediting charge transfer achieved by Bi2O3-modified TiO2 photocatalyst, Int. J. Hydrogen Energy 64 (2024) 842–852, https://doi.org/10.1016/j.ijhydene.2024.03.359.
[46] Z. Wei, J. Liu, W. Fang, M. Xu, Z. Qin, Z. Jiang, W. Shangguan, Photocatalytic hydrogen evolution with simultaneous antibiotic wastewater degradation via the visible-light-responsive bismuth spheres-g-C 3 N 4 nanohybrid: waste to energy insight, Chem. Eng. J. 358 (2019) 944–954, https://doi.org/10.1016/j.cej.2018.10.096.
[47] D. Sun, L. Huang, L. Li, Y. Yu, G. Du, B. Xu, Plasma enhanced Bi/Bi2O2CO3 heterojunction photocatalyst via a novel in-situ method, J. Colloid Interface Sci. 571 (2020) 80–89, https://doi.org/10.1016/j.jcis.2020.03.021.
[48] K. Annamalai, S. Vijayakumari, K.K. Kumar, N.R. Sasirekha, S. Balakumar, In situ nano-architectonic fabrication of Bi/BiOCl quasi-Ohmic heterojunctions via NaBH4 reduction for enhanced photo(electro)catalytic water remediation and splitting, Mater. Today Chem. 48 (2025) 102898, https://doi.org/10.1016/j.mtchem.2025.102898.
[49] W. Tang, L. Luo, Y. Chen, J. Li, Y. Dai, Y. Xie, Y. Ma, J. Zhang, Y. Zhang, Noble-metal-free Bi-OZIS nanohybrids for sacrificial-agent-free photocatalytic water

splitting: with long-lived photogenerated electrons, Sep. Purif. Technol. 357 (2025) 130047, https://doi.org/10.1016/j.seppur.2024.130047.
[50] Y. He, Y. Liu, Z. Zhang, X. Wang, C. Li, X.B. Chen, Z. Shi, S. Feng, Atomically dispersed bismuth on ZnIn2S4 Dual-Functional photocatalyst for photocatalytic hydrogen production coupled with oxidation of aromatic alcohols to aldehydes, Appl. Surf. Sci. 622 (2023) 156911, https://doi.org/10.1016/j.apsusc.2023.156911.
[51] W. Qin, Y. Xiao, C. Zhang, H. Gong, Q. Zhang, Q. Zeng, Bismuth nanocluster loaded on N-doped porous carbon with "memory catalysis" effect for efficient photocatalytic H2 generation and uranium(VI) reduction, Chem. Eng. J. 490 (2024) 151511, https://doi.org/10.1016/j.cej.2024.151511.
[52] L. Xu, W. qian Chen, S. qiang Ke, S. mei Zhang, M. Zhu, Y. Zhang, W. yan Shi, S. Horike, L. Tang, Construction of heterojunction Bi/Bi5O7I/Sn3O4 for efficient noble-metal-free Z-scheme photocatalytic H2 evolution, Chem. Eng. J. 382 (2020) 122810, https://doi.org/10.1016/j.cej.2019.122810.
[53] L. Geng, W. Li, X. Liu, X. Li, H. Fan, H. Qiu, X. Ma, M. Dong, Active sites modification and superior carriers separation synergistically boosted hydrogen production of Bi/Bi2MoO6/ZnIn2S4 non-noble metal S-scheme photocatalyst, J. Colloid Interface Sci. 629 (2023) 723–732, https://doi.org/10.1016/j.jcis.2022.09.029.
[54] Q. Shen, J. Chen, T. Wang, Y. Yang, C. Huang, W. Zhang, G. Tian, N. Cheng, S. Kai, Dual functional photocatalytic hydrogel coupled with hydrogen evolution and glucose depletion for diabetic wound therapy, J. Colloid Interface Sci. 695 (2025) 137753, https://doi.org/10.1016/j.jcis.2025.137753.
[55] S. Kampouri, K.C. Stylianou, Dual-functional photocatalysis for simultaneous hydrogen production and oxidation of organic substances, ACS Catal. 9 (2019) 4247–4270, https://doi.org/10.1021/acscatal.9b00332.
[56] W. Sun, Y. Zheng, J. Zhu, A " win-win " photocatalysis: coupling hydrogen production with the synthesis of high value-added organic chemicals, Mater. Today Sustain. 23 (2023) 100465, https://doi.org/10.1016/j.mtsust.2023.100465.
[57] K.E. Sanwald, T.F. Berto, A. Jentys, D.M. Camaioni, O.Y. Gutiérrez, J.A. Lercher, Kinetic coupling of water splitting and photoreforming on SrTiO3-based photocatalysts, ACS Catal. 8 (2018) 2902–2913, https://doi.org/10.1021/acscatal.7b03192.
[58] P. Zhang, T. Ochi, M. Fujitsuka, Y. Kobori, T. Majima, T. Tachikawa, Topotactic epitaxy of SrTiO3 mesocrystal superstructures with anisotropic construction for efficient overall water splitting, Angew. Chemie - Int. Ed. 56 (2017) 5299–5303, https://doi.org/10.1002/anie.201702223.
[59] H. Li, R. Li, G. Liu, M. Zhai, J. Yu, Noble-metal-free single- and dual-atom catalysts for artificial photosynthesis, Adv. Mater. 36 (2024), https://doi.org/10.1002/adma.202301307.
[60] F. Dong, Q. Li, Y. Sun, W. Ho, Noble metal-like behavior of plasmonic Bi particles as a cocatalyst deposited on (BiO)2CO3 microspheres for efficient visible light photocatalysis, ACS Catal. 4 (2014) 4341–4350, https://doi.org/10.1021/cs501038q.